Chemical Observations of a Polar Vortex Intrusion

M. R. Schoeberl, S. R. Kawa, A. R. Douglass, T. J. McGee

NASA Goddard Space Flight Center, Greenbelt, Md.

E. V. Browell

NASA Langley Research Center

Hampton, Va.

J. Waters, N. Livesey, W. Read, L. Froidevaux, M. L. Santee

NASA Jet Propulsion Laboratory, Pasadena, Ca.

H. C. Pumphrey

School of GeoSciences

The University of Edinburgh

Edinburgh, UK

L. R. Lait and L. Twigg

SSAI Corp.

Greenbelt, Md.

Abstract

An intrusion of vortex edge air into the interior of the Arctic polar vortex was observed on the January 31, 2005 flight of the NASA DC-8 aircraft. This intrusion was identified as anomalously high values of ozone by the AROTAL and DIAL lidars. Our analysis shows that this intrusion formed when a blocking feature near Iceland collapsed, allowing edge air to sweep into the vortex interior. Analysis of Aura MLS observations made along the DC-8 flight track also shows the intrusion in both ozone and HNO_3. Polar Stratospheric Clouds (PSCs) were observed by the DIAL lidar on the DC-8. The spatial variability of the PSCs can be explained using MLS HNO_3 and H_2O observations and meteorological analysis temperatures. We also estimate vortex denitrification using the relationship between N_2O and HNO_3. Reverse domain fill back trajectory calculations are used to focus on the features in the MLS data. The trajectory results improve the agreement between lidar measured ozone and MLS ozone and also improve the agreement between the HNO_3 measurements PSC locations. The back trajectory calculations allow us to compute the local denitrification rate and reduction of HCl within the filament. We estimate a denitrification rate of about 10%/day after exposure to below PSC formation temperature.

1. Introduction

The Arctic stratospheric polar vortex, unlike the Antarctic, exhibits both inward and outward wave breaking events [Plumb et al., 1994, hereafter P94]. Outward wave breaking is the term used to indicate erosion of the stratospheric polar vortex by mid-latitude wave breaking events [McIntyre and Palmer, 1983] and these events are commonly seen as the vortex erodes during winter [e.g. Schoeberl and Newman, 1996]. Inward wave breaking events occur when air moves into the vortex from mid-latitudes and is subsequently entrained and mixed within the vortex. Inside the vortex, the wind shear forms filaments that can be identified by composition that is not characteristic of the polar vortex.

In winter, as the polar vortex cools, sulfate aerosols swell and polar stratospheric clouds (PSCs) can form. These swollen sulfate aerosols and PSCs allow for the heterogeneous reaction of $ClONO_2$ and HCl to form Cl_2 and HNO_3, drawing down both chlorine reservoirs. Cl_2 photolyzes and reacts with ozone to form ClO which begins the catalytic destruction of ozone [Solomon, 1999]. There are three predominant types of PSCs in the lower stratosphere: ice which forms at temperatures below ~185K, nitric acid trihydrate (NAT) which forms near 195K, and swollen sulfate/nitric acid ternary aerosols that form near the same temperature as NAT. It is believed that rapid denitrification of the vortex can occur when ice clouds form [Fahey et al. 1990]. This is common in the Antarctic vortex. If temperatures below ~195K but above ice formation are sustained, large NAT

particles can also form and settle out gravitationally [Fahey et al., 2001], permanently removing HNO_3 and halting subsequent NAT formation. Aerosol lidars can be used to distinguish between the liquid aerosols, NAT and ice clouds using information from depolarization of the backscattered lidar beam and the wavelength dependence of the backscattering, which is representative of the size distribution of the aerosols [Browell et al., 1990a; Brooks et al., 2004].

The inward breaking events can alter the chemical composition of the vortex by replenishing ozone, nitric acid and the chlorine reservoirs. If inward breaking events occur, the correlations among the trace gases change, making ozone loss and denitrification more difficult to diagnose [Plumb et al., 2000].

P94 analyzed the inward breaking events observed during the 1992 AASE II aircraft experiment. This experiment took place a few months after the eruption of Mt. Pinatubo. The Pinatubo stratospheric aerosol cloud was not present when the Arctic polar vortex formed and thus the vortex was initially free of volcanic aerosol. During DC-8 flights through the vortex, the DC-8 DIAL lidar measurements showed Pinatubo aerosol intrusions into the vortex [P94]. These intrusions could be traced to an inward breaking event that occurred several days earlier. P94's analysis also showed that inward breaking events were not uncommon in the NH vortex but were almost never seen in the more stable Southern Hemisphere vortex. P94 discussed the dynamics of the event comparing various transport simulations with the lidar aerosol observations. P94 did not analyze ozone observations or assess the chemical implications of the inward breaking event.

Bird et al. [1997] analyzed ozone structures observed within the polar vortex using lidar and balloon measurements made near Eureka in the Canadian Arctic. Most of the laminae they observed in ozone were outside the vortex edge and appeared to be generated by the motion of the vortex. They also noted laminae within the vortex. The ozone laminae were correlated with the potential vorticity field and consistent with back-trajectory analysis.

Glatthor et al. [2005] used MIPAS data to analyze the chemistry of the unusual Antarctic vortex split of September 2002. They noted a strong correlation between MIPAS N_2O and PV. They also noted that the CH_4-N_2O correlation showed evidence of mixing into the Antarctic vortex during the period prior to the vortex break-up. This evidence appears as increased scatter in the correlation curve.

From mid-January to early February 2005, the Polar Aura Validation experiment (PAVE) conducted flights along the Aura sub-satellite track. On Jan. 31, 2005, ozone lidars on board a DC-8 flight north of Hudson Bay measured an anomaly in the stratospheric vortex ozone field suggesting the presence of vortex edge air within the polar vortex. This anomaly could be traced to an inward breaking vortex intrusion that occurred on Jan. 29, 2005. The Aura Microwave Limb Sounder (MLS) also observed the anomaly. In addition to the ozone filament, the lidars detected regions of Polar Stratospheric Clouds (PSCs) just south of the filament and co-located with the filament. The combined

measurements from the lidars, MLS and trajectory analysis provide a detailed chemical picture of the inward breaking event and also explain the spatial distribution of the PSCs.

2.0 The Vortex Intrusion

2.1 Potential vorticity

Fig. 1 shows the potential vorticity field at 480K from the Goddard Modeling and Assimilation Office GEOS-4 analysis [Bloom et al.., 2005; Douglass et al., 2003] as well as a 6-day reverse domain fill (RDF) analysis of the PV field [Sutton et al., 1994, Newman and Schoeberl, 1995]. RDF is a trajectory technique that provides an assessment of the unmixed transport. An *n*-day RDF uses *n*-day back trajectories from a given day. Mixing ratios of the trace gas at the earlier date are then interpolated onto the trajectory end points and copied forward along the trajectory path to describe the unmixed, non-reactive transported field.

The analysis field in Fig. 1a shows the vortex with a weak PV gradient near the east European sector (longitude ~45°). The RDF shows relatively low vorticity intruding into the vortex moving counter-clockwise around the pole. The flight track of the DC-8 is shown on the same figure. The northbound segment of the DC-8 flight follows the Aura ascending node orbit track. The flight was timed so that the Aura overpass occurred near the northern most part of the track. Because of this close coincidence we can assume that the DC-8 and MLS measurements are essentially simultaneous.

2.2 Ozone

Figure 2a shows AROTAL ozone observations made during the north-bound segment of the DC-8 flight. This ozone cross section was the same as observed by the DIAL ozone lidar also on the DC-8 (not shown). Because the DC-8 flight was made during the day to match the 1:30 PM Aura overpass time, the AROTAL instrument was operated primarily as an ozone differential absorption lidar and was not equipped for aerosol detection. Appendix I describes the AROTAL instrument in more detail. The DIAL lidar capabilities are described by Browell et al. [1990a, 1990b, 1993] and Brooks et al. [2004].

The AROTAL measurements are reported in geometric coordinates while MLS L2 data are reported in pressure coordinates. We have converted the AROTAL ozone and DIAL aerosol data (discussed later) to pressure coordinates using the geopotential height from the meteorological analysis. Hereafter we use log-pressure height ($7 \log_e(1000/p)$ km, where p is pressure in hPa) which we refer to as height. The vortex intrusion forms the filament outlined by the 3 ppmv contour line in the AROTAL data and MLS data (Fig. 2a, b). As expected the filament structure is more detailed in the AROTAL observations that are reported every 5 minutes with a vertical resolution of 0.75-3 km. MLS level 2 data are reported about every 1.5° degrees in latitude (this number decreases approaching the pole due to the orbital inclination) and the instrument has 2-3 km vertical resolution.

Appendix II describes the Aura MLS measurements in more detail, and AII.1 discusses MLS ozone.

Comparing Figures 2a and 2b, the filament observed by AROTAL is clearly evident in the MLS measurements, although the observations do not show the complex vertical and horizontal structure seen by both AROTAL and DIAL because of the lower spatial resolution of the MLS instrument. The filament also appears in MLS HNO_3 and N_2O measurements shown in Figures 7a and 10a, respectively, below. Using RDF calculations we can try and explain some of the structure shown in the lidar data. Figure 2c shows the 6-day RDF from MLS observations. The 3 ppmv contour in RDF can be compared to the same contour in the MLS and AROTAL. Figure 3 shows ozone values at 22 km, the MLS 4- and 6-day RDFs are able to capture the secondary filament (left arrow in the figure) not seen by MLS on January 31 but observed by AROTAL. The 6-day RDF seems to follow the AROTAL ozone measurements with slightly more fidelity than the 4-day RDF especially near the edge of the vortex (58ºN). From here on we will be using the 6-day RDF of the various trace gases.

Figure 4a shows the MLS ozone mapped to 480K potential temperature surface along with the MLS level 2 points and the DC-8 flight track. The map is created by averaging and linearly interpolating the level 2 data for each MLS level 2 pressure level onto a 2º latitude by 9º longitude grid. Using the GEOS-4 temperature analysis we then interpolate the data to the 480K surface. The 4 PVU contour is also shown (see Fig. 1) as a reference. The map shows that the highest ozone values are near the vortex edge where

diabatic descent is the strongest and ozone displaced downward relative to the exterior region as seen in Fig. 2. The filament observed by MLS is near 90ºW just north of the region where the outbound and return DC-8 flight tracks cross. The filament is not visible on the map due to the averaging. Using the MLS ozone map from six days earlier, we can construct a high resolution RDF of the ozone field. The RDF very clearly shows the ozone filament seen by MLS and AROTAL in Fig. 2b. The RDF shows that the high ozone filament is air drawn from the vortex edge and is brought around to the DC-8 flight track by the cyclonic circulation. The RDF ozone values are higher outside the vortex than the ozone map because MLS measurements six days earlier are higher. It is clear that inward breaking events that bring high ozone values into the vortex will make ozone loss calculations difficult.

2.3 Dynamics of the filament formation

P94 described the dynamics of filament formation for the case they studied. The vortex intrusions they described resulted from a blocking feature over the Northeast Atlantic that generated ridging in the lower stratosphere. In the winter 2004/5. a Northeast Atlantic blocking feature produced inward breaking events on December 29, January 16, January 31 and February 10. The blocking feature became so strong in late February that it caused the vortex to split on February 25 only to immediately rejoin when the block collapsed. By March 14 the vortex split again and never recovered. The dynamics of the filament formation in late January 2005 are very similar to the P94 case.

P94 discussed filament formation but did not discuss the role that the variability in the blocking feature plays in the formation of the filament. The sequence of events leading up to the formation of the filament is shown in Figure 5. The sequence begins with the strong blocking feature near zero longitude on January 28th (parts a, b) near Iceland. The map shows that this feature locally distorts the vortex; the vortex edge is displaced toward the pole. Then on January 29th, the blocking feature collapses (parts c, d). The vortex wind field becomes more zonal and begins to pull the edge material around into the vortex (parts e, f). The edge material then shears out and moves from Iceland to Northern Russia by Jan. 30 and is subsequently stretched out and carried around the pole. By January 31 the blocking ridge has reestablished itself.

To show that this process can bring edge material to the interior of the vortex, the trajectory of an air parcel is shown on the maps (Fig. 5 a,c,e,g). The parcel (small triangle) begins at the edge of the vortex on the 28th and by the 31st is well inside the main vortex at the location where the filament was observed. To summarize, it is the sequence of formation and collapse of the blocking ridge that leads to the filament development. The collapse of the blocking feature allows the vortex winds to sweep the edge air into the interior.

Over the course of the 2004/2005 winter, temperatures below NAT formation temperature first occur in early December. By very late December, the vortex cools to ice formation temperatures. At 480K, the vortex reaches ice formation temperatures sporadically throughout January and into mid February. The vortex warms up rapidly by

mid March. Over the course of the winter, the coldest temperatures are seen in a region that stretches from Hudson Bay to northern Norway across the North Atlantic. Fig. 6 shows the temperature field at 70ºN for late January. The 195K contour, which is a rough guide to the formation of PSCs is shown. The effect of the blocking ridge is to create a second cold pool over northern Hudson Bay. As the ridge collapses, the eastern cold pool warms. Note that very low temperatures persist over the North American sector during this period.

2.4 HNO_3 and PSCs

Fig. 7a shows the MLS cross section of HNO_3 along the DC-8 flight track. We note that MLS HNO_3 may be slightly high biased in the vortex (Appendix AII.2). The filament is clearly visible as a tongue of high HNO_3 near 65°N. DIAL lidar backscatter observations of PSCs from both the outbound and inbound flight tracks are overlaid on the HNO_3 field. The DIAL measures the aerosol backscattering ratio to molecular backscatter at 1064 nm with a vertical resolution of 75 m averaged over 4 second intervals. Brooks et al. [2004] discuss the DIAL lidar PSC detection capability in more detail. The location of the PSCs corresponds to regions of higher HNO_3 at toward the edge of the vortex and in the vicinity of the filament. High values of HNO_3 will increase the nitric acid trihydrate (NAT) formation temperature. These PSCs were identified as small solid particles, presumably NAT, based on depolarization. The backscatter ratios indicate that these were thin clouds with relatively low particle concentrations.

PSC formation can remove gas-phase HNO_3 either temporarily when HNO_3 is condensed or permanently when the condensate gravitationally settles out. Calculation of the NAT formation temperature from MLS observations of gas phase HNO_3 in the presence of condensate can lead to an underestimate that temperature. Fig. 7a shows contours of the NAT formation temperatures [Hanson and Mauersberger, 1988] using the GEOS-4 assimilated temperatures and MLS measurements of HNO_3 and H_2O (pink line). This figure shows that the area of PSCs formation temperatures include the PSC observations that coincide with the filament. However, the temperatures associated with the southernmost PSC patch are about 2K warmer than the formation temperature (dashed pink lines are T_{NAT}+2 K). To test whether the depletion in HNO_3 due to PSC formation affects our estimate of the PSC formation temperature, we have also computed PSC formation temperatures using HNO_3* which is derived from MLS N_2O (described below) and would not include PSC sequestered HNO_3. The results show only a very small shift in NAT formation temperature contours so we conclude that the PSCs are not sequestering a significant fraction of HNO_3 and that the southern PSC exists in a subsaturated environment. Model comparisons performed by Manney et al. [2005] for the Antarctic do not suggest a temperature bias in GEOS-4 of this magnitude.

Fig. 7b also shows the background HNO_3 and PSCs, but we have overlaid the contours of the number of days the air parcels have been exposed to sub-NAT formation temperatures using HNO_3 within the past 6 days. The contours line up well with the zone of highly depleted HNO_3 south of the filament. This suggests that this air was previously depleted of HNO_3 thus NAT formation temperatures are too low for PSC formation.

We have also computed the length of time since NAT temperatures were last reached. The southern patch of PSCs shown in the figure had seen PSC temperatures within 0.2 days suggesting that this feature, although occurring in a region where the formation temperatures are 2K above saturation, might be an evaporating remnant of a larger patch upwind. Fig. 7c shows a map of HNO_3 at the 480K surface. The southern patch of PSCs lies just leeward of the NAT saturation region (see the Montgomery stream function contours in Fig. 5g). This is consistent with the idea that winds might have advected the particles beyond the zone where temperatures are cold enough to form PSCs. Thus the southernmost NAT cloud might be particles that are in the process of evaporating.

To bring out the filament more clearly in the map we compute the 6-day RDF. Figure 8 shows maps of MLS HNO_3 on January 25 from which the Jan. 31 RDF is constructed. Note the very low HNO_3 region over Svalbard (or Spitzbergen, ~ 80ºN, 20º E) and the ring of high HNO_3 values at the vortex edge. Subsequent vortex motion pulls the edge HNO_3 into the long filament that creates the environment for the northernmost PSC patch. The RDF HNO_3 cross section (Figure 8c) shows even better alignment with the PSC features, and the other PSC zones line up better with the computed NAT+2K contours.

We also note that the RDF calculation show higher HNO_3 values above 20 km north of 70º N than were observed by MLS on January 31 (c.f., Figure 7a). The direct MLS observations of very low HNO_3 are consistent with the lack of lidar PSC observation in this region. This difference suggests that air north of 70º N has been denitrified between

Jan. 25 and the 31st. Indeed, at 480K, temperatures were below ice formation values over Svalbard from 25-27 January. An ice event like this would have quickly expanded the region of denitrifed air in the polar region.

2.5 Denitrification

Gao et al. [2001] noted that ozone loss within the Arctic vortex is a strong function of the level of denitrification with higher ozone loss occurring in significantly denitrified air masses. Using MLS HNO_3, N_2O and trajectories we can estimate denitrification. N_2O can be used to compute initial NO_y that in this region is mostly in the form HNO_3. Using aircraft, satellite, and balloon observations, the relationship between N_2O and NO_y has been described by Fahey [1990], Chang et al. [1996], and Kondo et al. [1996]. These papers used this relationship to estimate denitrification within the polar vortex. However, the relationship between N_2O and NO_y is not linear, and mixing events can create a new relationship as discussed by Plumb et. al. [2000] and Esler and Waugh [2002]. Plumb et al. [2000] pointed out that mixing events between deep vortex air masses with very low NO_y and vortex edge air masses with higher NO_y may confuse the expected signal of PSC denitrification. Plumb et al. [2003] showed in more detail how mixing and descent in a model that lacked PSC denitrification processes can produce alternative N_2O and NO_y relationships that appear to show denitrification even though none occurred. Using multiple tracers, permanent denitrification by PSCs can be estimated [Rex et al.,1999; Esler and Waugh, 2002], but without additional tracers that procedure cannot be applied here.

To check on the relationship between NO_y and N_2O, Fig. 9 shows 5 day averages of level 2 MLS N_2O and HNO_3 from 60º N to the pole, 20-25 km, averaged into 5 ppbv N_2O bins during different periods of vortex evolution. The date indicates the first day of the 5 day data group. Although there is considerable scatter in the data (not shown), the expected non-linear relationship emerges. We note how this relationship changes as the season evolves, especially for values of N_2O below about 200 ppbv. Values of N_2O above 200 ppbv at 480K are found well outside the vortex. Climatologically, most dramatic vortex descent takes place during the fall and early winter so we expect little upper stratospheric air to arrive inside the vortex after December 15. The first intrusion event occurs on December 29, and, although, minimum NH temperatures in 2004-2005 at 50 mbar first go below T_{NAT} on about December 4 the vortex cold pool is not very extensive until after mid-December. Thus changes in the relationship between N_2O and HNO_3 after December 15 should be due to mixing within the vortex itself, intrusions into the vortex or heterogeneous processes affecting HNO_3.

The curve in the <200 ppbv region flattens out with time. This behavior is consistent with the description of subsequent mixing of air within the vortex described by Plumb et al. [2002]. Nonetheless, after January 31 we see a general decrease in HNO_3 in the <200 ppbv of N_2O zone. The overall drop in HNO_3 between January 31 and February 15 suggests permanent denitrification by PSCs rather than mixing because after March 15 minimum temperatures within the vortex were above PSC formation temperatures so the PSCs would have evaporated. Thus similarity between the March 15 curve and the

February 15 curve confirms the fact that the denitrification is not due to sequestration by PSCs.

Denitrification can be estimated either using the difference (HNO_3-HNO^*_3) or by using an earlier estimate of HNO_3 and trajectory mapping (appropriate for recent denitrification) to estimate a percentage change. We use the relationship between HNO_3 and N_2O on December 15, 2004 (Fig. 9) to compute the change in HNO_3 for reasons discussed above.

There are several possible causes for a local change in HNO_3 within the vortex: (1) mixing of low HNO_3 air inside the vortex and higher HNO_3 air inside the vortex as described by Plumb et al. [2000], (2) entry of high HNO_3 vortex edge air into the vortex, (3) sequestration or evaporation of HNO_3 in PSCs which may fall out of the stratosphere, (4) photolysis, (5) descent from above, (6) formation of HNO_3 by the reaction of HCl with $ClONO_2$. Photolysis of HNO_3 at these sun angles can be neglected, and formation from $ClONO_2$ can only change HNO_3 by few ppbv. Vortex increases in HNO_3 near 20 km will thus be produced by mixing, descent, evaporation of PSCs, and through entry of edge air. Increased HNO_3 via sedimentation and evaporation has been observed at altitudes below about 15 km [Koike et al., 2001]. Vortex decreases in HNO_3 can be produced by mixing and by PSC condensation.

Fig. 10a shows MLS N_2O (Appendix AII.4) from which HNO_3^* is derived and the difference between HNO_3 and HNO_3^* - or the net change in HNO_3 since Dec. 15, 2004.

PSCs were not observed north of 70º so the denitrification in that region appears to be permanent. Fig. 10b also shows a smaller denitrified region corresponding to the low HNO_3 air at 63ºN discussed in the last section.

Overall there appears to be a net decrease in 18-22 km HNO_3 throughout the vortex. This change could not occur simply through internal vortex mixing. Fig. 10c confirms the overall decrease of HNO_3 compared to HNO_3* at 480K within the vortex, and these changes roughly line up with the coldest temperatures. Below 400K and north of 60ºN there is a net increase in HNO_3 (Fig. 10b) that might be due to evaporation of NAT as they fall into warmer regions below.

To estimate how fast PSCs might be denitrifying the filament we can compare PSC temperature exposure history against local denitrification over the last 6 days. PSC formation temperatures computed using MLS HNO_3 and H_2O and back trajectories are used to link Jan. 31 and Jan. 25 points. We restrict our analysis to the filament region inside the small box shown in Fig. 10b. PSC backscatter occurs in this region but the PSC amount is very small. This is air that has been exposed to low temperatures but was not initially denitrified. The results are shown in Fig. 11. The figure shows that HNO_3 depletion does not show up immediately. Instead it increases with below-PSC temperature exposure but only after 3 days. After 3 days, the rate is roughly 10%/day of exposure. The temperature history of these parcels shows that the temperature was above ice formation temperature during this period. The large standard deviation of these measurements probably reflects the sensitivity of PSC formation to microphysical

processes [Drdla et al., 2002]. Carslaw et al. [2002] modeled the formation of large NAT particles that were observed during SOLVE [Fahey et al., 2001] and concluded that the denitrification by these particles took place over eight days, a longer period than available here. Since small amounts of NAT are clearly still present in the filament air mass, we have to conclude that denitrification within the filament may be ongoing.

2.6 HCl and ClO measurements

Since PSCs were observed in the filament, heterogeneous chemical processing of the chlorine reservoirs should have taken place. Fig. 12 plots the HCl and ClO observed by MLS over the DC-8 track (see Appendix AII.3 and AII.5 for a discussion of these measurements). In Fig. 12a HCl is strongly depleted inside the vortex region, even within the filament. As expected, ClO is very high throughout the whole region including the filament. Using the back trajectories, we can compute the change in HCl from MLS observations six days earlier. This is shown in Fig 12c. Recent depletion in the filament region near 66° N is evident. In addition, we see HCl depletion occurring near the outer regions of the vortex.

The highest levels of ClO are collocated with the zone of highly denitrified air at 63ºN. Even though Fig. 10b shows more denitrified air further north, the higher solar zenith angles in that region reduces ClO concentrations. The lack of HNO_3 in this air mass will slow the conversion of ClO back to $ClONO_2$ and thus produce maximum potential for ozone loss [i.e., Gao et al. 2002].

3.0 Summary

We describe the chemical structure of an inward breaking filament in the northern winter vortex. Such an event was first identified and described by P94 using aerosol observations. Here we use both aircraft and satellite observations to describe a filament that was observed on the DC-8 flight of Jan. 31, 2005. The filament was observed by AROTAL ozone lidar measurements and was also seen in the MLS ozone and HNO_3 observations. The AROTAL ozone lidar shows a complex ozone anomaly well within the vortex. The MLS level 2 observations show the filament as a broader feature as might be expected given the lower MLS vertical and horizontal resolution. The trajectory calculations show that the filament originated from air near the edge of the vortex.

We discuss the process of filament formation. As with the case studied by P94, this filament owes its existence to a blocking ridge near Iceland. The collapse of this ridge allows vortex edge material to be brought inward and be advected around inside the vortex.

Of special interest is the observation of PSCs by the DC-8 DIAL lidar. The intermittent PSC observations are analyzed with regard to HNO_3 and the temperature history of the air parcels. The HNO_3 observations show that the location of the PSCs correlates with air that has not been significantly denitrified. The southern PSC region along the flight is associated with vortex edge air. The northern region is associated with the filament. The

two PSC regions are separated by about 400 km of highly denitrified air. Using MLS HNO_3* (computed from N_2O) we are able to produce denitrification maps of the whole vortex region. From the HNO_3 loss in the filament we estimate the denitrification rate is about 10% per day after three days when temperatures are below PSC formation threshold. There is no evidence of a filament in MLS HCl. This suggests that HCl has already been converted to active chlorine and is consistent with MLS ClO measurements.

The combination of MLS ozone, HNO_3, N_2O, HCl and ClO along with aircraft ozone and PSC observations provide a very complete picture of the filament chemistry.

Acknowledgments

The authors would like to thank the NASA HQ, NASA Dryden and NASA Ames groups for outstanding support during the Polar Aura Validation Experiment (PAVE). Some of this work was performed while the first author was visiting the College of Oceanic and Atmospheric Sciences at Oregon State University. This work was supported by NASA's Earth Science Program.

Appendix I The AROTAL Instrument

The AROTAL lidar consists of a pair of lasers: a frequency-tripled Nd-YAG laser emitting ~225 mJ at 355 nm and a 50 Hz pulse repetition rate; and a 200Hz XeCl excimer laser emitting ~200 mJ at 308 nm. Because of physical constraints, the transmitted beams

are not expanded and are transmitted co-axially with the receiver telescope. The 308 nm radiation is absorbed by ozone and ozone absorption at 355 nm is negligible. These wavelengths are particularly well suited for lidar measurements of stratospheric ozone.

The primary receiver is a zenith viewing 16" f/3 Newtonian telescope mounted beneath a 16" viewing port in the aircraft fuselage. Although two wavelengths are transmitted, four wavelengths are received. In addition to the two elastically scattered returns at 308 and 355 nm, N_2 Raman-scattered returns from each of these transmitted wavelengths are recorded at 332 nm and 387 nm. Extremely high solar backgrounds, coupled with the comparatively weak Raman signals meant that these channels were largely inoperative during the PAVE campaign. The elastic returns are spectrally separated and power-split into three phototubes for each elastic wavelength. This preserves the linearity of the signal, as the lidar return can vary over five orders of magnitude in this configuration. The photomultiplier tubes are blocked from the low altitude, high intensity initial return, to essentially remove signal-induced noise [McGee et al,. 1995]. In addition to the three detectors looking at returns collected through the 16" telescope, each of the elastic wavelengths makes use of two independent, small aperture, large field-of-view mini-receivers to bring a linear lidar return as close to the aircraft skin as possible. These mini-receivers are mounted inside the main telescope, over top of the beam transmission tubes, and produce no further obscuration of the primary telescope.

The lidar data is acquired in 15 m bins, which are read out every 20 seconds. These 20-second data sets are integrated for 3-5 minutes, and a running mean ozone profile is

obtained and displayed every 20 seconds. The 15 m vertical bins are integrated and reported in the data archive on 150 m centers. The actual vertical resolution of retrieved ozone varies with altitude above the aircraft between 0.75 – 3 km. The algorithm used to compute ozone profiles is the same as that developed for the GSFC ground-based instrument. This algorithm has undergone two algorithm comparisons [Godin et al. 1999; T. Leblanc, personal communication] and has been validated in numerous international campaigns.

Appendix II Aura MLS Data

The Aura MLS instrument and data are described in Waters et al. [2006] and the specifics of the level 2 data are described in JPL publication D-32381 available at http://mls.jpl.nasa.gov. We use version 1.5 of the data. The relevant portions of the JPL publication have been extracted, edited and reproduced below.

AII.1 Ozone

The standard product for version 1.5 O_3 is taken from the 240 GHz retrieval. This product has the highest sensitivity down into the upper troposphere, as well as in the mesosphere. The recommended vertical range is 215- 0.46 hPa. Retrieval simulations indicate that the average biases are small over the vertical range recommended above, with overall accuracy (closure) of better than 1%, not a major error source, and there is excellent tracking between the simulated retrieval results and the true input profiles. An iterative full forward model is used for increased accuracy over a broad altitude range.

The estimated precision for stratospheric ozone compares well with the RMS scatter about the truth. Simulations indicate good closure for O_3 in the upper troposphere, typically to better than 10%. The vertical resolution for the standard O_3 product is 3 km in the upper troposphere and lower stratosphere, but degrades to 4 km at 215 hPa and 6 km in the mesosphere. The estimated single-profile precision reported by the Level 2 software typically varies from 0.2 - 0.4 ppmv (or 2 to 15 %) from the mid-stratosphere to the lower mesosphere. The observed scatter in the data, evaluated in a narrow latitude band centered around the equator where atmospheric variability is expected to be small, tends to be slightly larger than these values. This scatter is larger than the estimated precision by 30% near the ozone peak, and by a factor of more than two near 100 hPa. Some of this may be caused by atmospheric variability, as well as by smoothing constraints (used for the a priori profile). The early O_3 comparisons [Froidevaux et al., 2005] indicate overall agreement at roughly the 5 - 10% level with stratospheric profiles from SAGE II, HALOE, POAM III, and ACE. MLS ozone values tend to be slightly higher than the occultation data sets in the lower stratosphere, and slightly low in the upper stratosphere, but the degree of `tilt' in this slope of the average differences changes from one comparison to the next, indicating that there are also differences between the occultation data sets themselves (see Froidevaux et al. [2005] for more details).

AII.2 HNO_3

The standard product for version 1.5 HNO_3 is taken from the 240 GHz retrieval at and below 10 hPa, and from the 190 GHz retrieval at and above 6.8 hPa. The vertical

resolution of the standard HNO_3 product is estimated to be 3.5 km over the range 147 to 10 hPa, degrading to 4.5 km at 3.2 hPa. Over most of the recommended vertical range, the estimated single-profile precision reported by the Level 2 software varies from 1.0 to 1.5 ppbv; the observed scatter in the data, evaluated in a 20º -wide latitude band centered around the equator where atmospheric variability is expected to be small, suggests a measurement precision of 1 ppbv throughout the profile. Preliminary comparisons with a climatology based on seven years of UARS MLS HNO_3 measurements [Santee et al., 2004] suggest that EOS MLS HNO_3 may be biased high by several ppbv near the profile peak. Much closer agreement with the UARS climatology is generally found at other latitudes/altitudes/seasons. Comparisons of HNO_3 profiles from MLS and ACE at middle and high latitudes in both hemispheres over the January to March 2005 time period [Froidevaux et al., 2005] indicate that, in an average sense, MLS HNO_3 is high relative to ACE by at least 2 - 3 ppbv (30%) at the levels surrounding the profile peak. Average agreement between the two satellite measurements is better (typically within 10%) near the top and bottom of the profile. Despite the apparent offset between MLS and ACE near the profile peak, however, comparisons of nearly coincident individual measurements show good agreement in capturing the overall shapes of the HNO_3 profiles and tracking variations in them. Comparisons with HNO_3 measurements from the FIRS-2 and Mark-IV instruments obtained during a balloon campaign from Ft. Sumner, NM in September 2004 lead to similar conclusions: MLS mixing ratios exceed those measured by the balloon instruments by as much as 3 ppbv at the levels around the profile peak, with agreement typically much better at the top and bottom of the vertical range [Froidevaux et al., 2005]. The discrepancies between HNO_3 abundances measured by

MLS and those measured by ACE, FIRS-2, and Mark-IV may arise in part because of uncertainties in either the infrared or the microwave spectroscopy; this possibility is under investigation. The altitude, latitude, and seasonal dependence of the apparent high bias in the MLS version 1.5 HNO_3 data will be explored in more detail in future validation studies, both through analysis of potential shortcomings in the MLS retrieval system and comparisons with additional correlative (ground-based, aircraft, balloon, and satellite) data sources.

AII.3 HCl

The standard product for version 1.5 HCl is taken from the 640 GHz retrieval. The vertical resolution for HCl is ~3 km in the lower stratosphere, and degrades to 5 - 6 km near 1 hPa and 7 km at the top recommended level of 0.2 hPa. The estimated single-profile precision ranges from 0.1 ppbv (lower stratosphere) to 0.5 ppbv (lower mesosphere), or 5 -15 %. This is typically close to the scatter based on the retrieved profile variability, evaluated in a narrow latitude band centered around the equator, where atmospheric variability is expected to be small, except at the top end of the profile, where the scatter tends to be somewhat smaller than the estimated precision; this indicates an increasing influence from the *a priori*, although not to an extent that affects the retrieved abundances much. Comparisons of MLS and HALOE HCl for January-March, 2005 [Froidevaux et al., 2005] indicate that MLS HCl abundances are typically high, relative to HALOE, by 0.2 to 0.4 ppbv (10 to 15%). In contrast, MLS HCl is typically within 5% of the ACE HCl values, certainly in the upper stratosphere and in the more quiescent SH

lower stratosphere. Larger differences are observed in the more disturbed conditions of NH high latitude winter. The exact cause of the disagreement with HALOE is not known at this time, but there have been indications that HALOE HCl data were on the `low side' of other observations (from satellite, balloons, aircraft) by 10 - 15%. Comparisons of MLS HCl versus balloon-borne measurements in September 2004 from Ft. Sumner, New Mexico, indicate good agreement, generally within the combined random errors. Despite the bias issue versus HALOE, we find that the HCl latitudinal variations agree well between HALOE and MLS.

AII.4 N_2O

The standard product for v1.5 N_2O is taken from the 640 GHz retrieval. The results of simulations are show reported precision for N_2O of around 20 ppbv in the mid-stratosphere, corresponding to about 10%. The precision is poorer in the lowermost stratosphere and also worsens in the upper stratosphere. This reported precision overestimates the scatter seen in retrieval simulations by about 50%. The simulations show that average biases are typically under 10%, although individual points in the lower stratosphere can show biases as large as 100% in the winter polar vortex conditions. The vertical resolution for v1.5 N_2O is around 2 - 3 km in most of the stratosphere and lower mesosphere, worsening to 5 - 6 km in the lowermost stratosphere and at 0.1 hPa and above.

Initial comparisons with observations from the ACE instrument show mean biases of

around 20%, and 40% scatter or better in the lower stratosphere. Comparisons of MLS N_2O observations with balloon borne observations are very encouraging, showing agreement within the expected levels of precision.

AII.5 H_2O

The standard water vapor product is taken from the 190 GHz retrieval. It is unusual among MLS products in that it is assumed that log(Mixing ratio), and not mixing ratio itself, varies linearly with log pressure. For this reason, scientific studies considering averages of MLS water vapor data should perform the averaging in log space. The scatter in the data is much smaller than the precision estimate. This is because the radiance errors provided to the retrieval formula are inflated to as much as 2 K. This is done to account for unexplained systematic errors that would otherwise cause poor convergence in the retrieval. The vertical resolution for H2O is 2.7 - 3 km at pressures greater than 100 hPa, increases to 4 km for pressures less than 46 hPa, remaining constant throughout the stratosphere and degrades to 6 km and 7 km near 1 hPa and 0.1 hPa (the top recommended level), respectively.

The data have been compared [Froidevaux et al., 2005] to data from four occultation instruments: ACE, HALOE, POAM III and SAGE II. The comparison is qualitatively good, but the MLS data generally show a small positive bias: 5 - 10% against HALOE, 0 - 5% against ACE and 10 ñ 15% against SAGE II. The bias is negative, about 10- 20%, against POAM III. Agreement against the Mk IV and

FIRS-2 balloon instruments is also good.

AII.6 ClO

The standard product for ClO is taken from the 640 GHz retrieval. ClO is strongly diurnal in the lower stratosphere; day-night differences can be used to reduce systematic effects in the measurements from 100 to 10 hPa. The ClO vertical resolution varies with altitude, from 3 km over the range 100 to 10 hPa to 5 km near the top of the profile.

The estimated single-profile precision reported by the Level 2 software varies from 0.15 to 0.2 ppbv over the range 100 to 10 hPa, degrading to 0.4-0.5 ppbv near 1 hPa. The observed scatter in the data, evaluated in a 20 -wide latitude band centered around the equator where natural variability is expected to be small in the lower stratosphere, suggests a measurement precision of 0.1-0.2 ppbv throughout the profile. Comparisons with correlative data sources have not yet been undertaken for ClO, so accuracy estimates are not available. However, time series of daytime, nighttime, and day-night difference values from almost nine months of version 1.5 data have been examined in 5º -wide equivalent latitude bands between 87.5º S and 87.5º N on the 660, 580, 520, 460, and 410 K potential temperature surfaces (corresponding to pressure levels of 22, 32, 46, 68, and 100 hPa, respectively). At the topmost level, nighttime mixing ratios are approximately zero at all equivalent latitudes and seasons for both ClO products. At the lower levels, however, a persistent negative bias of as much as 0.3 ppbv is evident at low and middle latitudes in both daytime and nighttime mixing ratios from the ClO-640 GHz retrievals.

At polar latitudes, the ClO-640GHz nighttime mixing ratios temporarily exhibit non-negligible positive values during the winter when ClO is enhanced; at other seasons a negative bias comparable to that always present at low and middle latitudes is seen. Taking day-night differences in the lower stratosphere effectively eliminates the negative bias; it also leads to reduced ClO mixing ratios during the winter enhancement at polar latitudes, since nighttime values are slightly positive at that time/location.

References

Bird, J. C. et al., Observations of ozone structure in the Arctic polar vortex. *J. Geophys. Res.* 102, 10785-10800, 1997.

Bloom, S. et al. , Documentation and Validation of the Goddard Earth Observing System (GEOS) Data Assimilation System - Version 4. Technical Report Series on Global Modeling and Data Assimilation 104606, 26, 2005.

Brooks, S.D., et al., Polar stratospheric clouds during SOLVE/THESEO: Comparison of lidar observations with in situ measurements, *J. Geophys. Res.,* **109**, D02212, 2004.

Browell, E. V., C. F. Butler, S. Ismail, P. A. Robinette, A. F. Carter, N. S. Higdon, O. B. Toon, M. R. Schoeberl, and A. F. Tuck, Airborne lidar observations in the wintertime Arctic stratosphere: Polar stratosphere clouds, *Geophys. Res. Lett.*, **17**, 385-388, 1990a.

Browell, E. V., C. F. Butler, S. Ismail, M. A. Fenn, S. A. Kooi, A. F. Carter, A. F. Tuck, O. B. Toon, M. H. Proffitt, M. Loewenstein, M. R. Schoeberl, I. Isaksen, and G. Braathen, Airborne lidar observations in the wintertime Arctic stratosphere: Ozone, *Geophys. Res. Lett.*, *17*, 325-328, 1990b.

Browell, E. V., C. F. Butler, M. A. Fenn, W. B. Grant, S. Ismail, M. Schoeberl, O. B. Toon, M. Loewenstein, and J. R. Podolske, Ozone and aerosol changes observed during the 1992 Airborne Arctic Stratospheric Expedition, *Science*, *261*, 1155-1158, 1993.

Carslaw K. S., et al.. A vortex-scale simulation of the growth and sedimentation of large nitric acid hydrate particles, *J. Geophys. Res.*, **107**, 8300, 2002.

Chang, A. Y., et al., A comparison of measurements from ATMOS and instruments aboard the ER-2 aircraft: Tracers of atmospheric transport, *Geophys. Res. Lett.*, 23, 2389-2392, 1996

Drdla, K., M. R. Schoeberl and E. V. Browell, Microphysical modeling of the 1999-2000 Arctic winter: 1. Polar stratospheric clouds, denitrification, and dehydration, *J. Geophys. Res.*, 108, 8312, 2002.

Douglass, A. R., M. R. Schoeberl, R. B. Rood, and S. Pawson, Evaluation of transport in the lower tropical stratosphere in a global chemistry and transport model, *J. Geophys. Res.*, 108, 2003.

Esler, J. G., D. W. Waugh, A method for estimating the extent of denitrification of Arctic polar vortex air from tracer-tracer scatter plots, *J. Geophys. Res.*, 107, 4169, 2002.

Fahey, D., et al., Observations of denitrification and dehydration in the winter polar stratosphere, *Nature*, 344, 321-344, 1990.

Fahey DW, et al., The detection of large HNO_3-containing particles in the winter arctic stratosphere, *Science*, 291, 1026-1031, 2001

Froidevaux, L. et al. Early validation analyses of atmospheric profiles from EOS MLS on the Aura satellite. *IEEE Transactions on Geoscience and Remote Sensing*, (in press) 2005.

Gao RS, et al., Observational evidence for the role of denitrification in Arctic stratospheric ozone loss, *Geophys. Res. Lett.*, 28, 2879-2882, 2001.

Glatthor et al., Mixing processes during the Antarctic vortex split of September-October 2002 as inferred from source gas and ozone distributions from ENVISAT-MIPAS, *J. Atmos. Sci.*, 62, 787-800, 2005.

Godin, S., et al., Ozone differential absorption lidar algorithm intercomparisons, *Applied Optics*, 38**,** 6225 - 6236, 1999.

Hanson, D. and K. Mauersberger, Solubility And Equilibrium Vapor-Pressures Of HCl Dissolved In Polar Stratospheric Cloud Materials - Ice And The Trihydrate Of Nitric-Acid**,** *Geophys. Res. Lett.*, 15, 1507-1510, 1988.

Koike, I. H., Y. Kondo, G. E. Bodeker, M. Y. Danilin, and Y. Sanso, Redistribution of nitric acid in the Arctic lower stratosphere during the winter of 1996-97, J. Geophys. Res., 106, 23139,-23150, 2001.

Kondo, Y. et al., NOy correlation with N_2O and CH_4 in the mid-latitude stratosphere, *Geophys. Res. Lett.*, 23, 2369-2372, 1996.

Manney et al., Diagnostic comparison of meteorological analyses during the 2002 Antarctic winter, Mon. Wea. Rev., 133, 1261-1278, 2005.

McGee, T. J., M. Gross, U.N. Singh, J. J. Butler, and P. Kimvilakani, An Improved Stratospheric Ozone Lidar, *Opt. Engin.,* **34,** 1421-1430, 1995.

Newman, P. A. and M. R. Schoeberl, A Reinterpretation of the Data from the NASA Stratosphere-Troposphere Exchange Project, *Geophys. Res. Lett.*, **22**, 2501-2504, 1995.

Plumb, R. A. et al. Intrusions into the lower stratospheric Arctic vortex during the winter of 1991-1992, *J. Geophys. Res.,* **99**, 1089-1105, 1994.

Plumb, R. A., D. W. Waugh, M. P. Chipperfield, The effects of mixing on tracer relationships in the polar vortices, *J. Geophys. Res.*, 105(D8), 10047-10062, 10.1029/1999JD901023, 2000.

Plumb, R. A. et al., Global tracer modeling during SOLVE: High-latitude descent and mixing, *J. Geophys. Res.*, 108, 8309, 2003.

Rex, M. et al. Subsidence, mixing, and denitrification of Arctic polar vortex air measured During POLARIS, *J. Geophys. Res.*, 104, 26611-26623, 1999.

Santee, M. L., G. L. Manney, N. J. Livesey, and W. G. Read. Three-dimensional structure and evolution of stratospheric HNO3 based on UARS Microwave Limb Sounder measurements. *J. of Geophys. Res.*, 109:D15306, 2004. doi:10.1029/2004JD004578.

Schoeberl, M. R. and P. A. Newman, A Multiple Level Trajectory Analysis of Vortex Filaments, J. Geophys. Res., 100 , 25801-25815, 1996.

Solomon, S., Stratospheric ozone depletion: A review of concepts and history, *Rev. Geophys.* 37, 275-316, 1999.

Sutton, R. T., H. MacLean, R. Swinbank, A. O'Neill, and F. W. Taylor, High-resolution stratospheric tracer fields estimated from satellite observations using Lagrangian trajectory calculations, *J. Atmos. Sci.*, *51*, 2995-3005, 1994.

Waters, J., et al., The Earth Observing System Microwave Limb Sounder (EOS MLS) on the Aura Satellite, IEEE Trans. Geosci. and Remote Sensing, (in press), 2006.

Figure Captions

Figure 1. Part a is the analyzed potential vorticity field north of 30º N at 480K on January 31, 2005 units of $x10^{-5}$ $Km^2/kg/s$ or 1 PVU. The dark line shows the flight track of the DC-8 on the same day. Pink line is the 4 PVU contour approximately indicating the vortex edge. Part b is the 6-day RDF generated using the PV field from 6 days earlier.

Figure 2. Ozone mixing ratio measured by the AROTAL lidar (a) and MLS (b) along the DC-8 flight track in ppmv. Parts a and b show the potential temperature surfaces interpolated from the meteorological analysis onto the DC-8 flight track. The black line shows the 3 ppmv contour in part a. Note the high ozone values north of 60ºN between 20 and 25 km; these are the ozone filaments discussed below. In part b, the MLS 3 ppmv line is solid while the AROTAL line is dashed. In part c, a 6-day RDF ozone calculation is shown, the orange line is the 3 ppmv RDF contour, the thick black line is MLS data, the thin black line is AROTAL data.

Figure 3. Plots of ozone at 22 km from AROTAL, MLS and the 4- and 6-day MLS RDF calculations. The arrows indicate the locations of the filaments.

Figure 4. Ozone at 480 K observed by MLS. Black line shows the DC-8 flight track. Black dots show the MLS observation points. Blue line is the 4 PVU contour (see Fig. 1). Part a, observations on Jan. 31, 2005; Part b, 6 day RDF on Jan. 31, 2005 that uses MLS data from Jan. 25, 2005.

Figure 5. The sequence of events leading up to the formation of the vortex filament on Jan. 31, 2005 is shown. Maps show the 480K potential vorticity map in PVU units. Black contours show the Montgomery stream function. Black ring shows the location of the corresponding zonal cross section contour plots. The small triangle on the maps represents the back trajectory location of a parcel starting at the observation point on Jan 31. Contour plots show the zonal variation of the perturbation geopotential height (GPH) at 70ºN times 100m. The 480K surface is shown as the thick black curve.

Figure 6. Perturbation temperature (temperature minus its zonal mean) around the 70º N contour. The thick white line is the 480K potential temperature contour. The thick black line is the 480K potential temperature contour.

Figure 7. Parts a and b show the MLS HNO_3 along the flight track in ppbv. Black contours are potential temperature surfaces. Dashed black contours are temperature in Part a. White contours along the cross section show the location of enhanced backscatter

ratio from the DIAL lidar from both outbound and inbound tracks; the contours are 1.5, 2.0, 3.0 and 4.0 times enhanced aerosol over molecular back scatter. In Part a, pink lines are the NAT formation temperature based on MLS HNO_3 and H_2O; dashed pink lines are NAT+2K. In Part b, the contours show total exposure to the sub-NAT formation temperatures in days during the last 6 days. Part c shows a map of MLS HNO_3 on the 480K surface. The 4 PVU level is shown in blue. The NAT formation temperature contour is the dashed line. DIAL PSC locations at 480K are shown as white regions on the DC-8 flight track which is shown in black.

Figure 8. Part a shows MLS HNO_3 interpolated onto the 480K for January 25. Part b shows the 6 day RDF formed from the observations of January 25. The pink line is the 4 PVU contour. The DC-8 flight track in shown in black with the white regions corresponding to PSC regions. Part c shows the Jan. 31 RDF cross section of HNO_3. The temperature contours are black dotted lines. The pink line shows the NAT formation contour using RDF MLS HNO_3, RDF H_2O and assimilated temperatures, the dashed pink line is NAT + 2K.

Figure 9. HNO_3 vs N_2O relationship computed from the MLS level 2 data from 60ºN to the pole from 20-25 km for several dates (YYMMDD) showing the evolution of the relationship. See text for details.

Figure 10. Part a, MLS N_2O along the flight track which is used to compute HNO_3*; pink line shows the 50 ppbv contour for reference. Part b, HNO_3*-HNO_3. basically the

change HNO_3 since December 15, 2004. Temperature history contours are also shown (see Fig 7b) white contours areas correspond to high aerosol backscatter. White box is the region used to generate Fig. 11. Part c, map of the change in HNO_3 at 480K. Blue line is the 4 PVU contour. Black lines are temperature contours from 190K to 198K every 2K.

Figure 11. Recent denitrification computed as the percent difference between the initial and finalized values of HNO_3 at the beginning and end of a 6-day trajectory associated with the filament. Exposure is time the parcel has encountered below PSC temperatures over the last six days using MLS HNO_3 and H_2O observed at the start of the trajectory. Error bars indicate one standard deviation in the ensemble of points for each bin.

Figure 12. Part a, HCl, along the DC-8 flight track from the MLS data. Yellow lines show the PSC exposure time as in Fig. 7b. Pink contour shows the 3 ppmv MLS ozone contour. Part c shows the HCl depletion computed using 6 day back trajectories.

Jan 31, 2005 480K PV

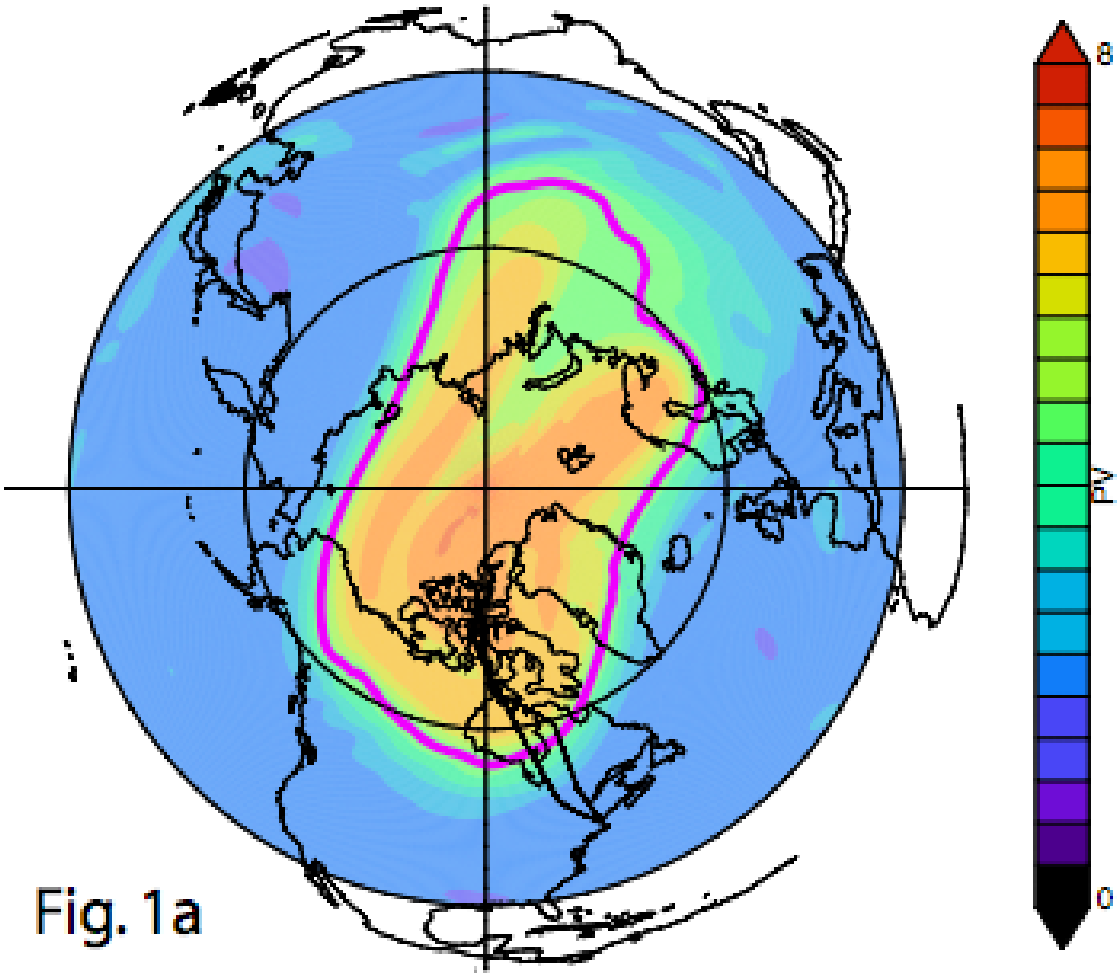

Fig. 1a

6-day RDF Jan 31,2005

480K

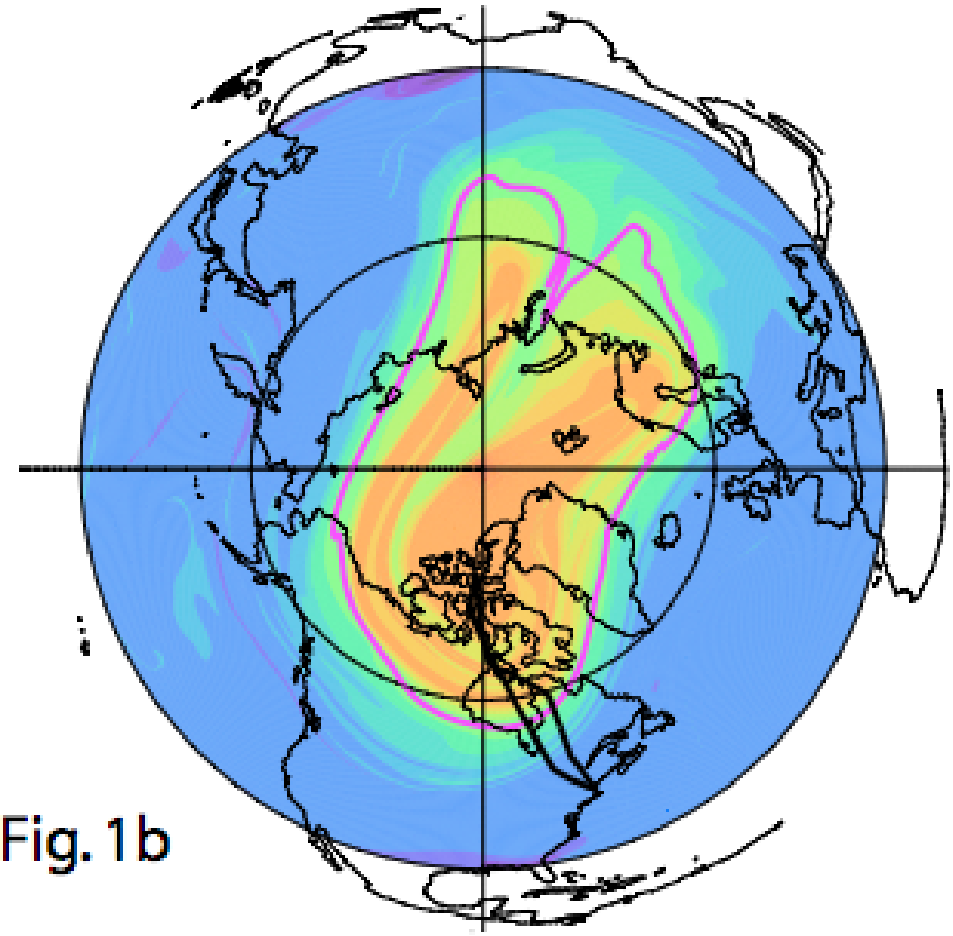

Fig. 1b

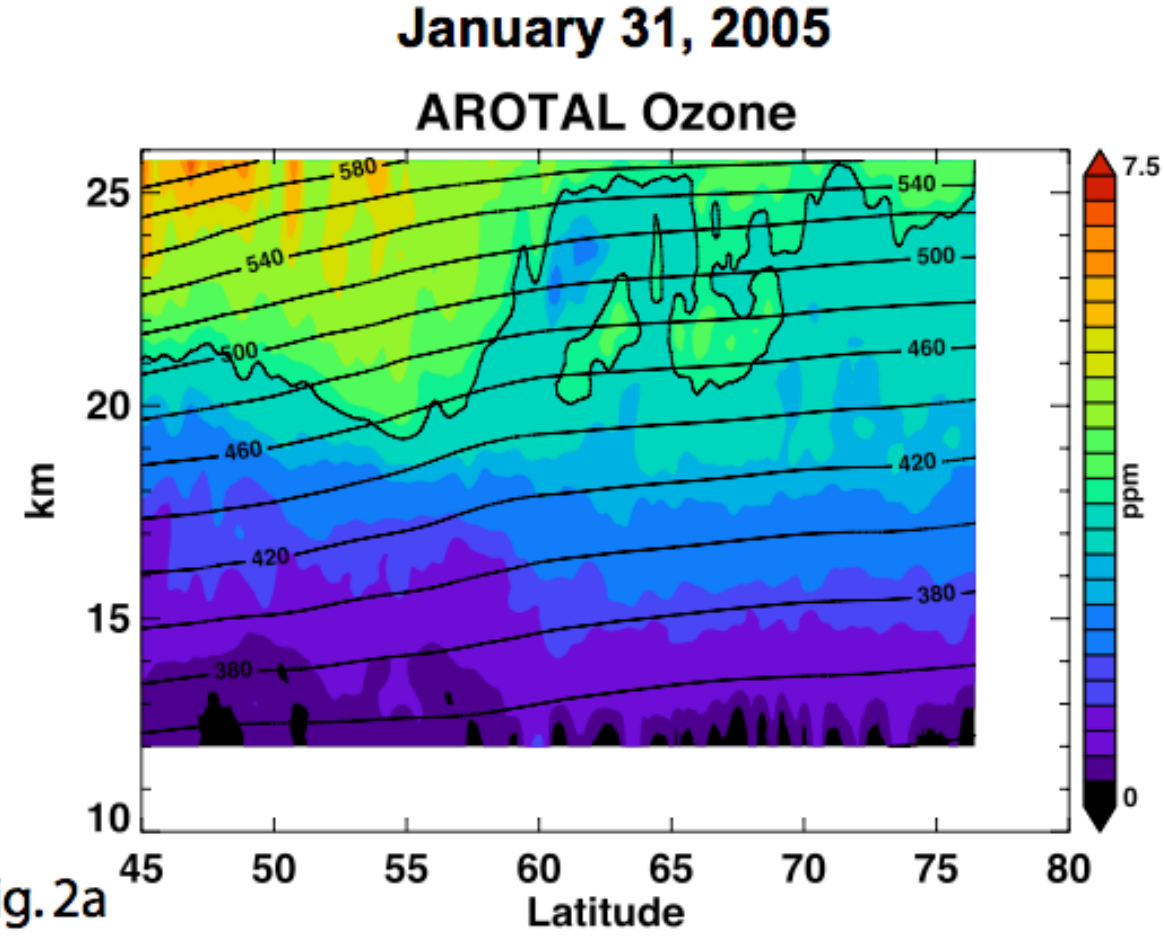
January 31, 2005
AROTAL Ozone
km
25
20
15
10
580
540
500
460
420
380
45
50
55
60
65
70
75
80
Latitude
7.5
ppm
0

Fig. 2a

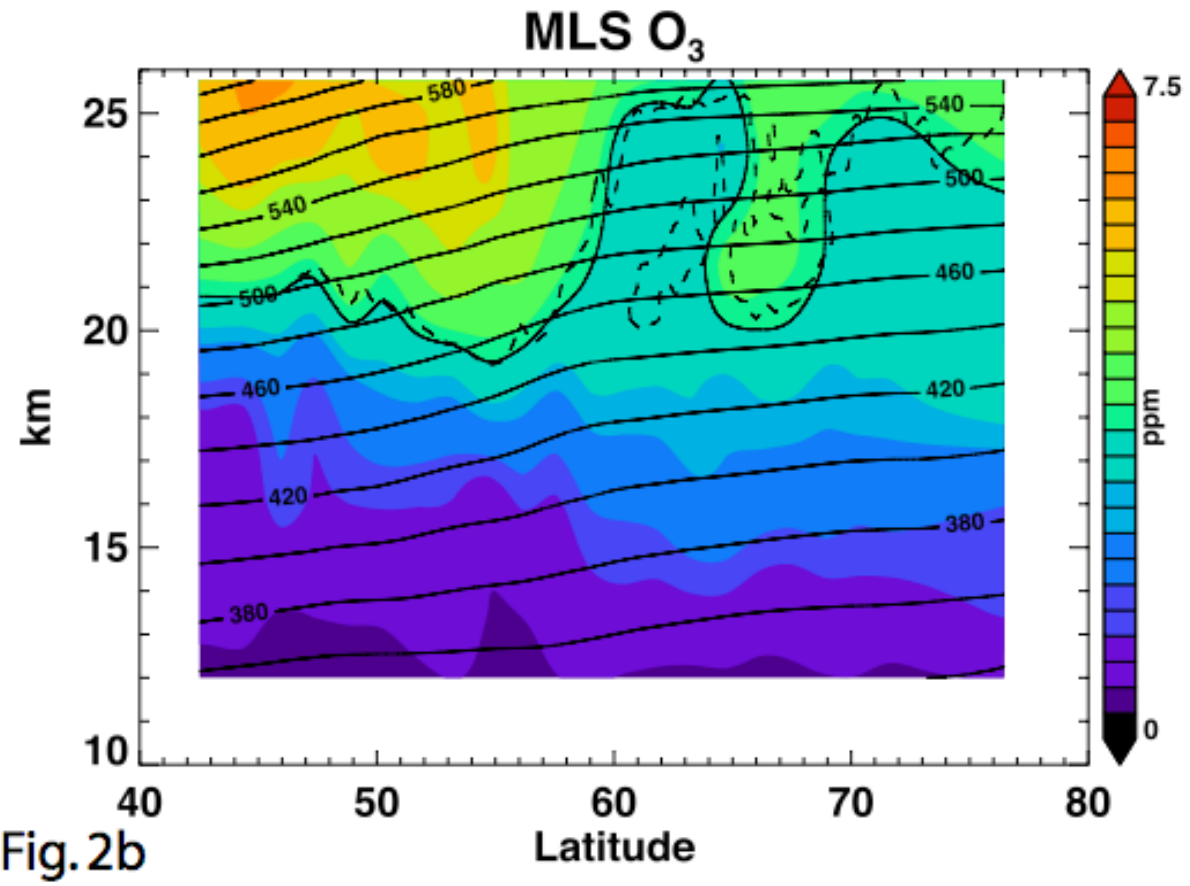
MLS O3
580
540
500
460
420
380
km
25
20
15
10
40
50
60
70
80
Latitude
7.5
ppm
0

Fig. 2b

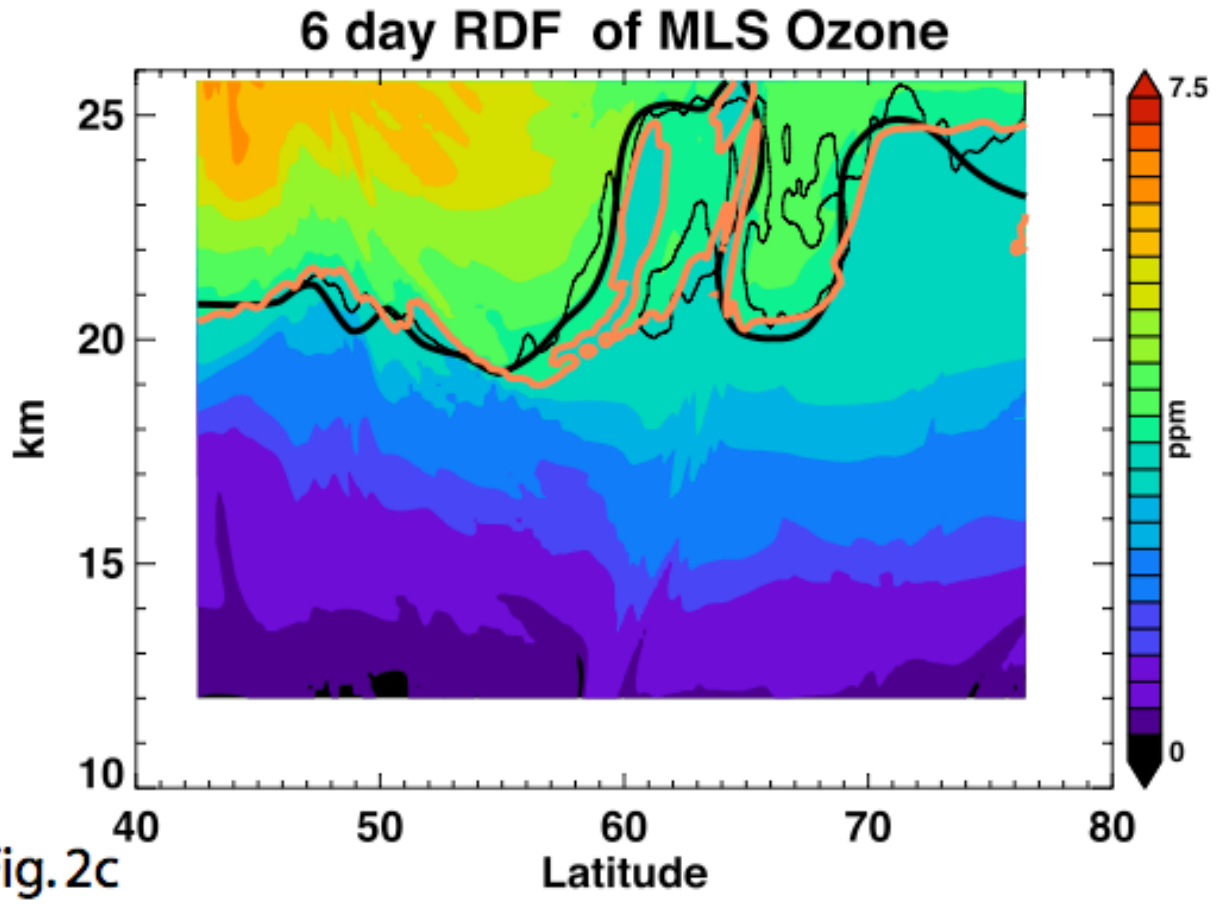
6 day RDF of MLS Ozone
25
20
15
10
km
40
50
60
70
80
Latitude
7.5
ppm
0

Fig. 2c

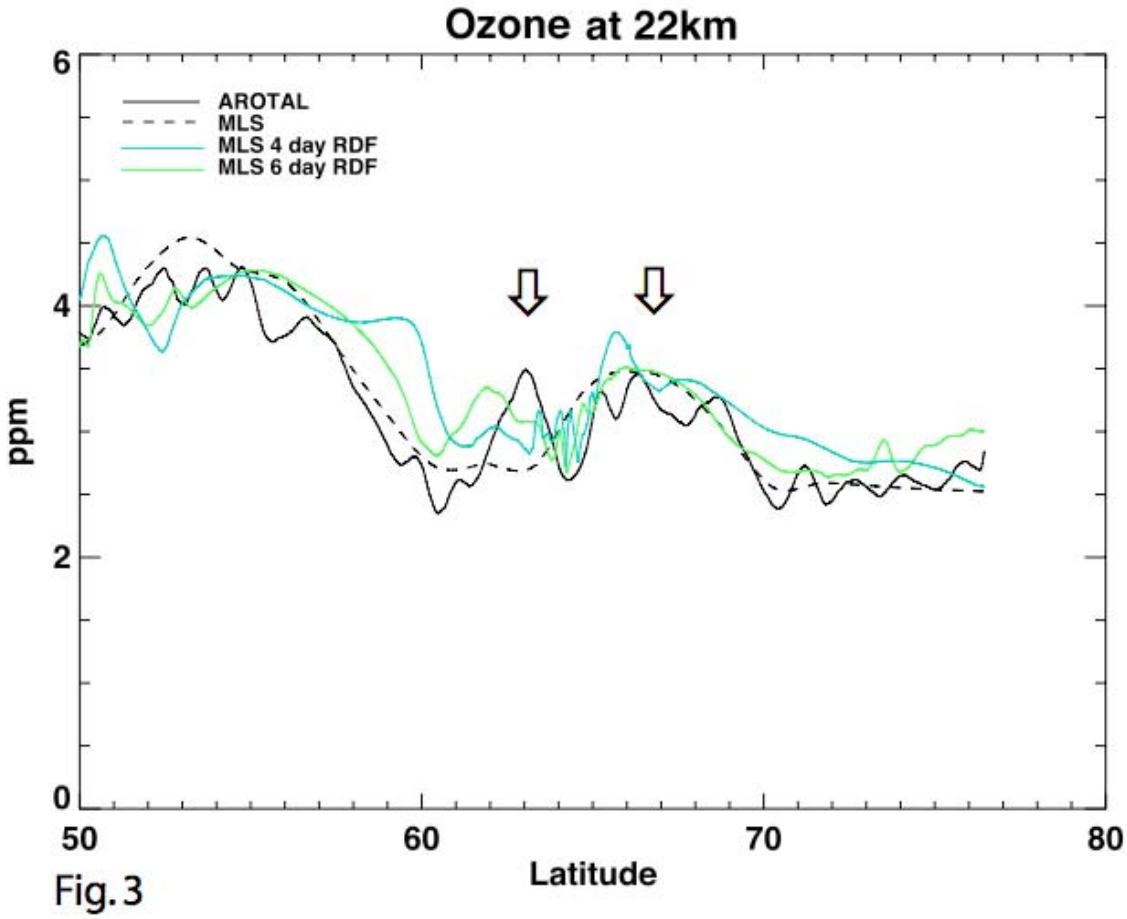
Ozone at 22km
AROTAL
MLS
MLS 4 day RDF
MLS 6 day RDF
ppm
6
4
2
0
50
60
70
80
Latitude

Fig. 3

MLS O_3 480K, Jan 31, 2005

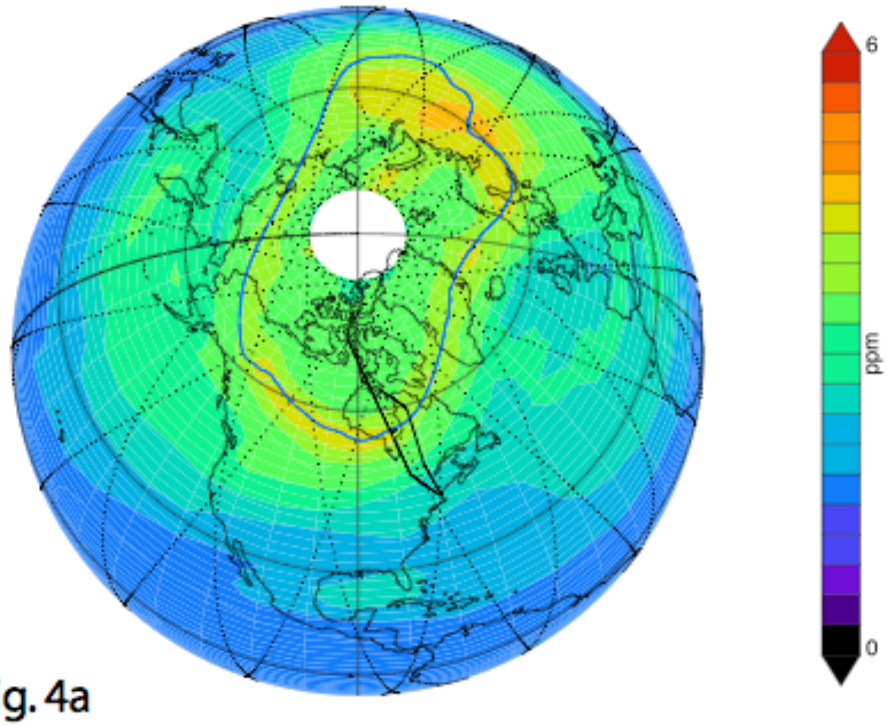

Fig. 4a

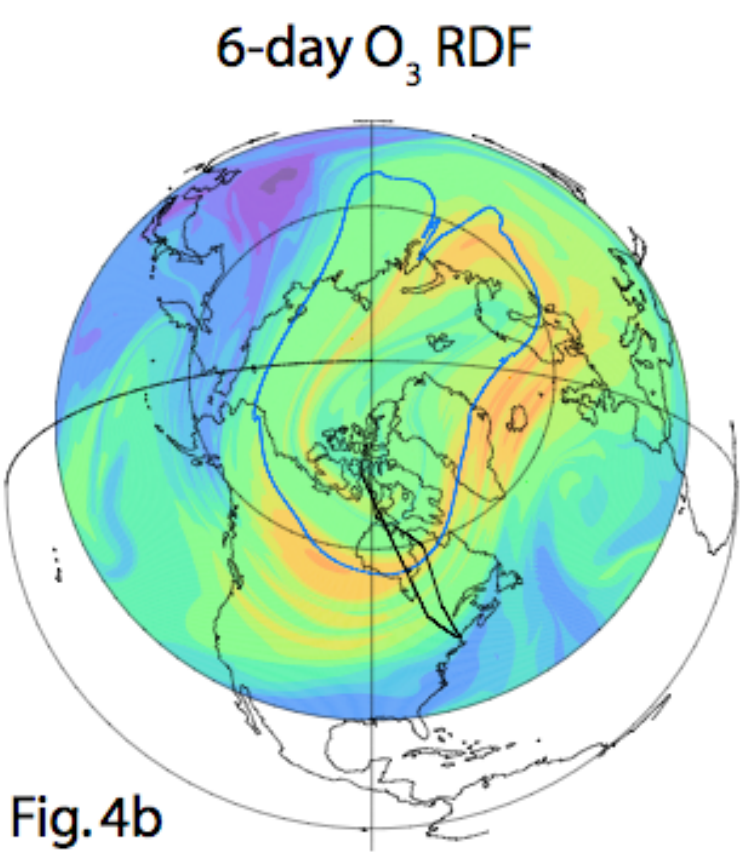

Fig. 4b

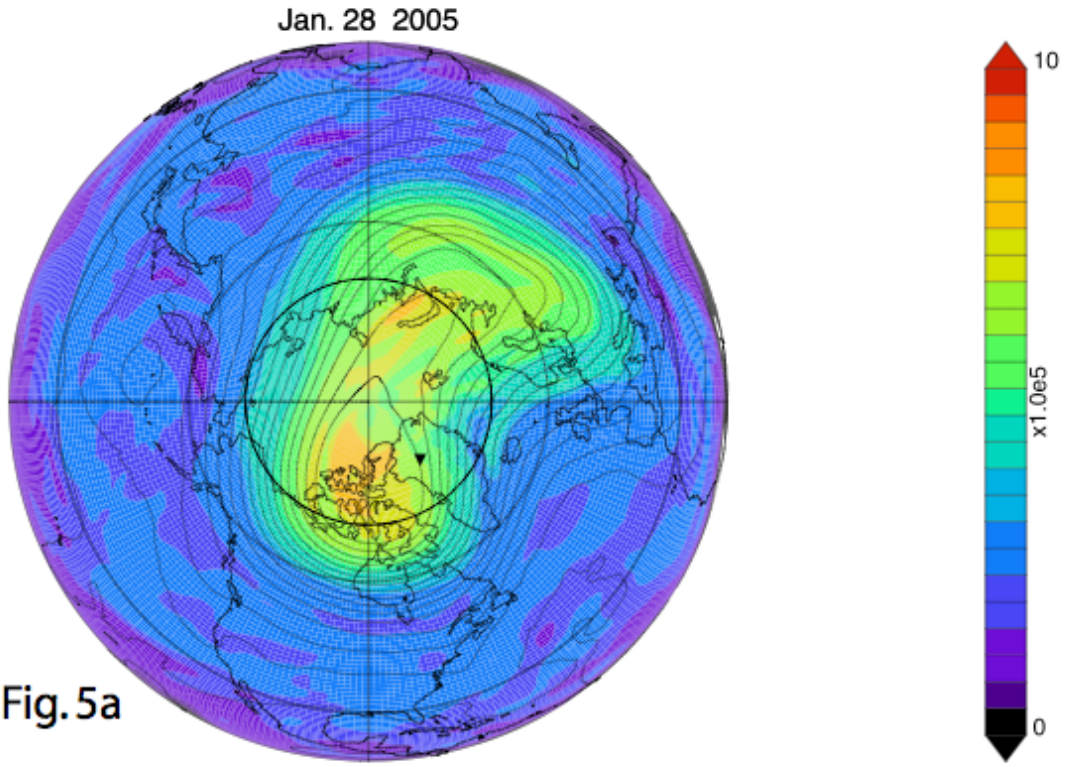

Fig. 5a

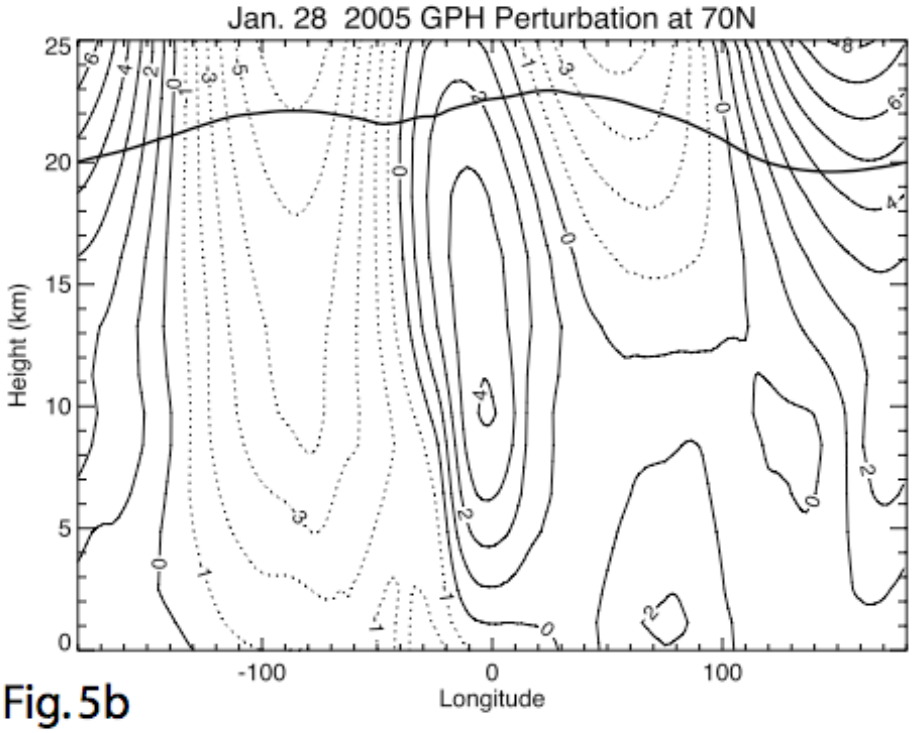
Jan. 28 2005 GPH Perturbation at 70N
Height (km)
25
20
15
10
5
0
-100
0
100
Longitude

Fig. 5b

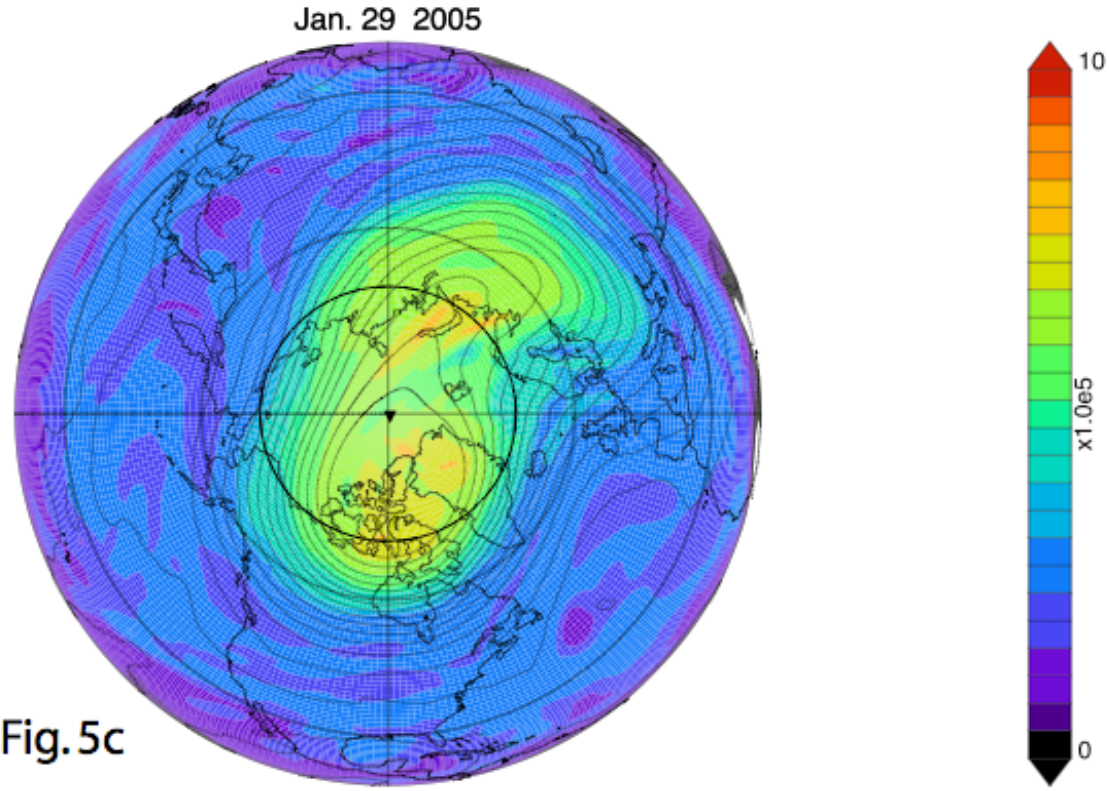

Fig. 5c

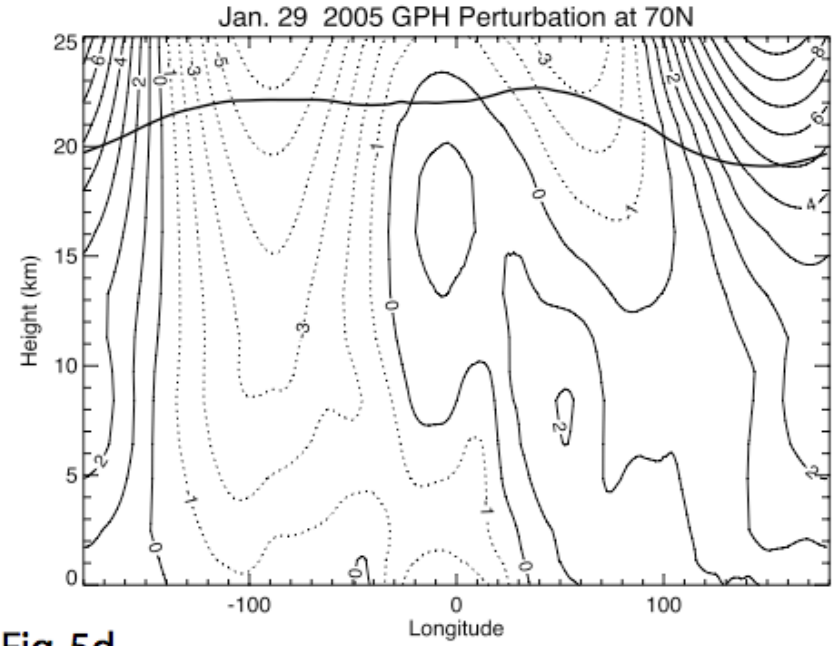
Jan. 29 2005 GPH Perturbation at 70N
Height (km)
Longitude
25
20
15
10
5
0
-100
0
100

Fig. 5d

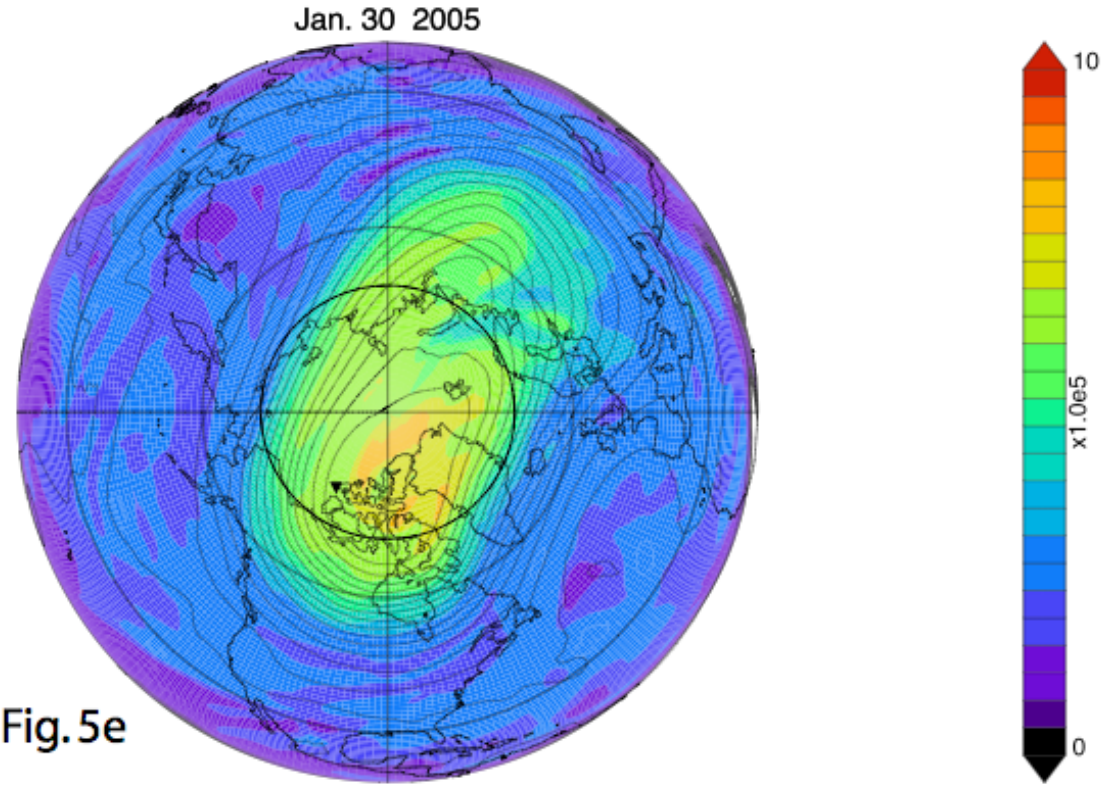
Jan. 30 2005
10
x1.0e5
0

Fig. 5e

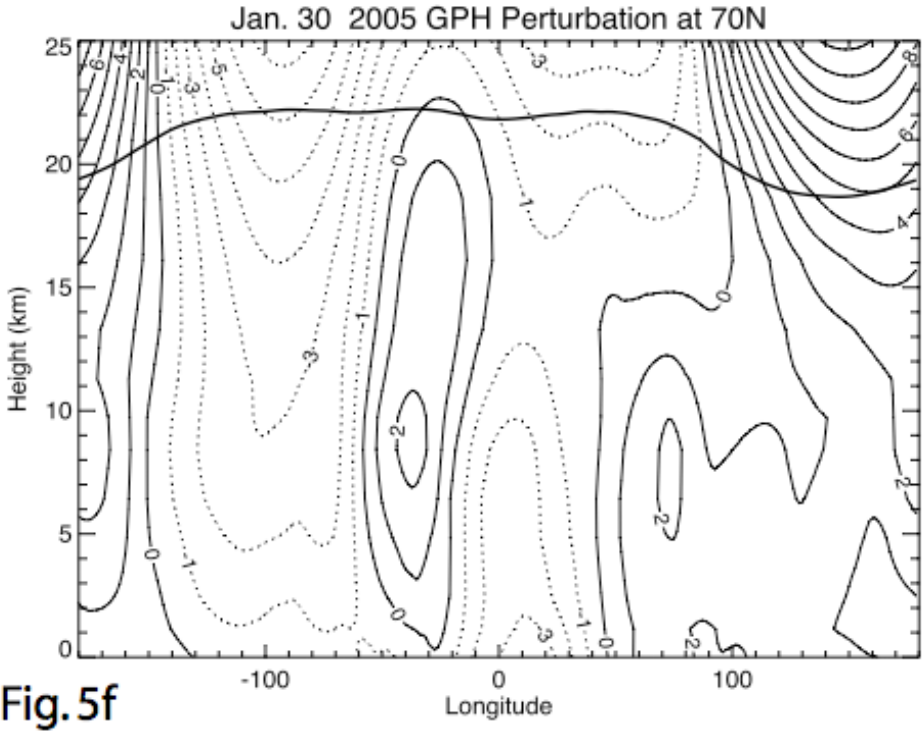
Jan. 30 2005 GPH Perturbation at 70N
Height (km)
25
20
15
10
5
0
-100
0
100
Longitude

Fig. 5f

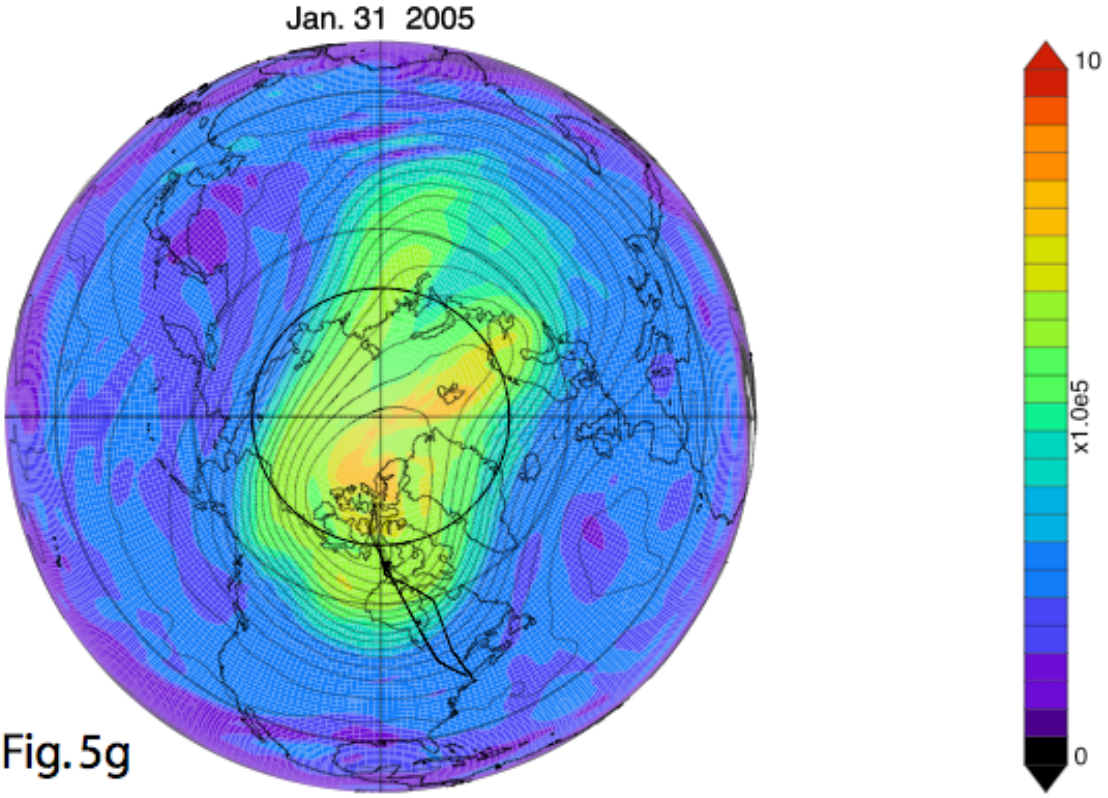
Jan. 31 2005
10
x1.0e5
0

Fig. 5g

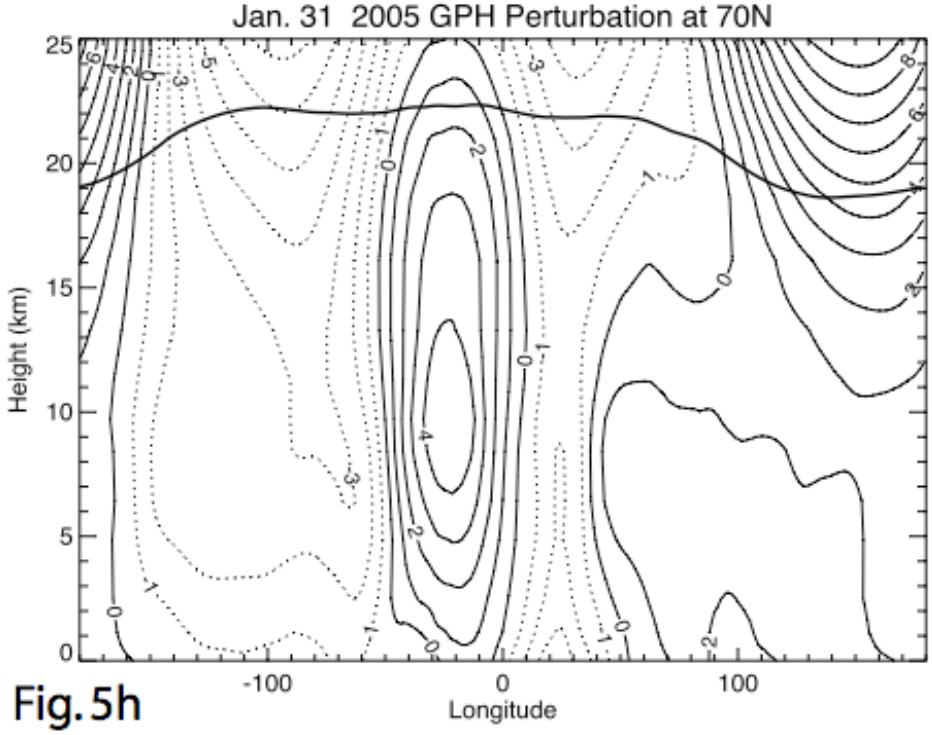
Jan. 31 2005 GPH Perturbation at 70N
Height (km)
25
20
15
10
5
0
-100
0
100
Longitude

Fig. 5h

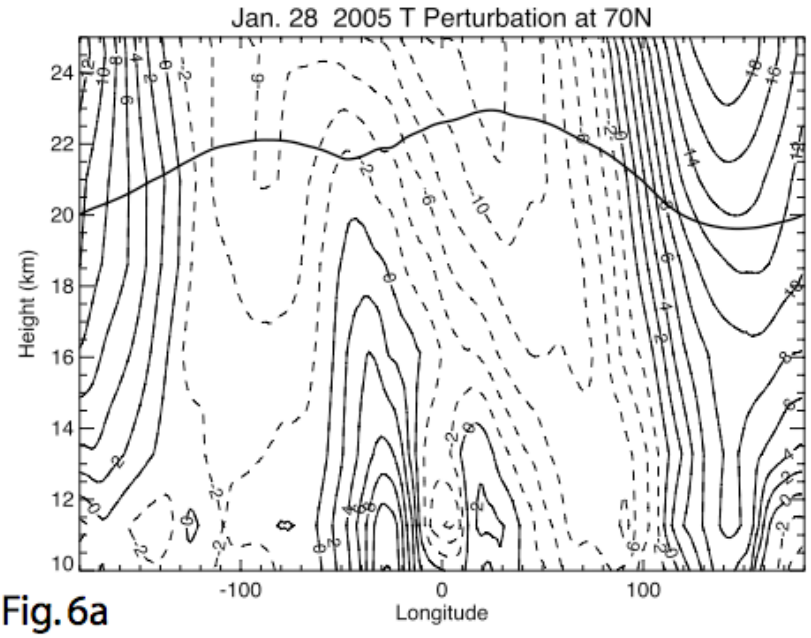
Jan. 28 2005 T Perturbation at 70N
Height (km)
Longitude
24
22
20
18
16
14
12
10
-100
0
100

Fig. 6a

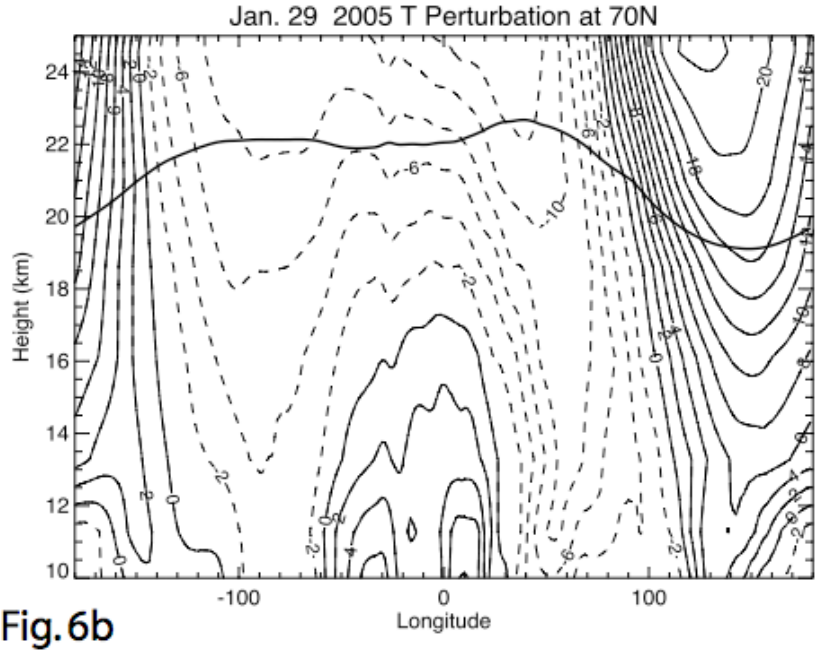
Jan. 29 2005 T Perturbation at 70N
Height (km)
Longitude
24
22
20
18
16
14
12
10
-100
0
100

Fig. 6b

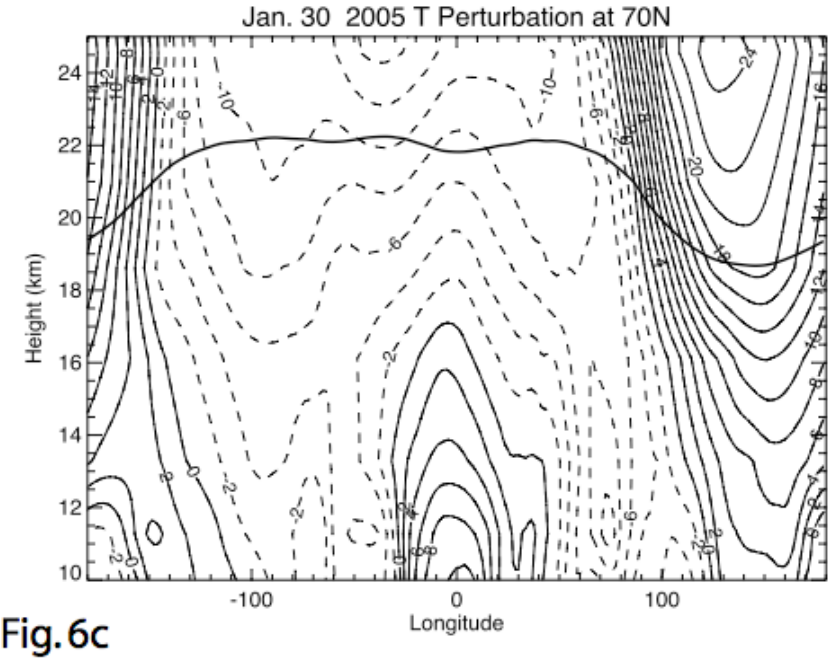
Jan. 30 2005 T Perturbation at 70N
Height (km)
Longitude
24
22
20
18
16
14
12
10
-100
0
100

Fig. 6c

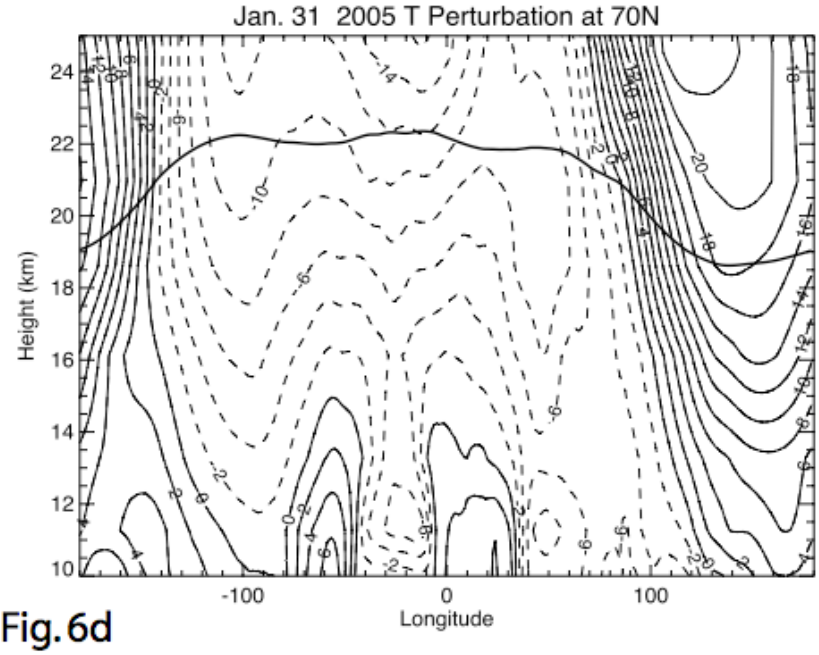
Jan. 31 2005 T Perturbation at 70N
Height (km)
Longitude
24
22
20
18
16
14
12
10
-100
0
100

Fig. 6d

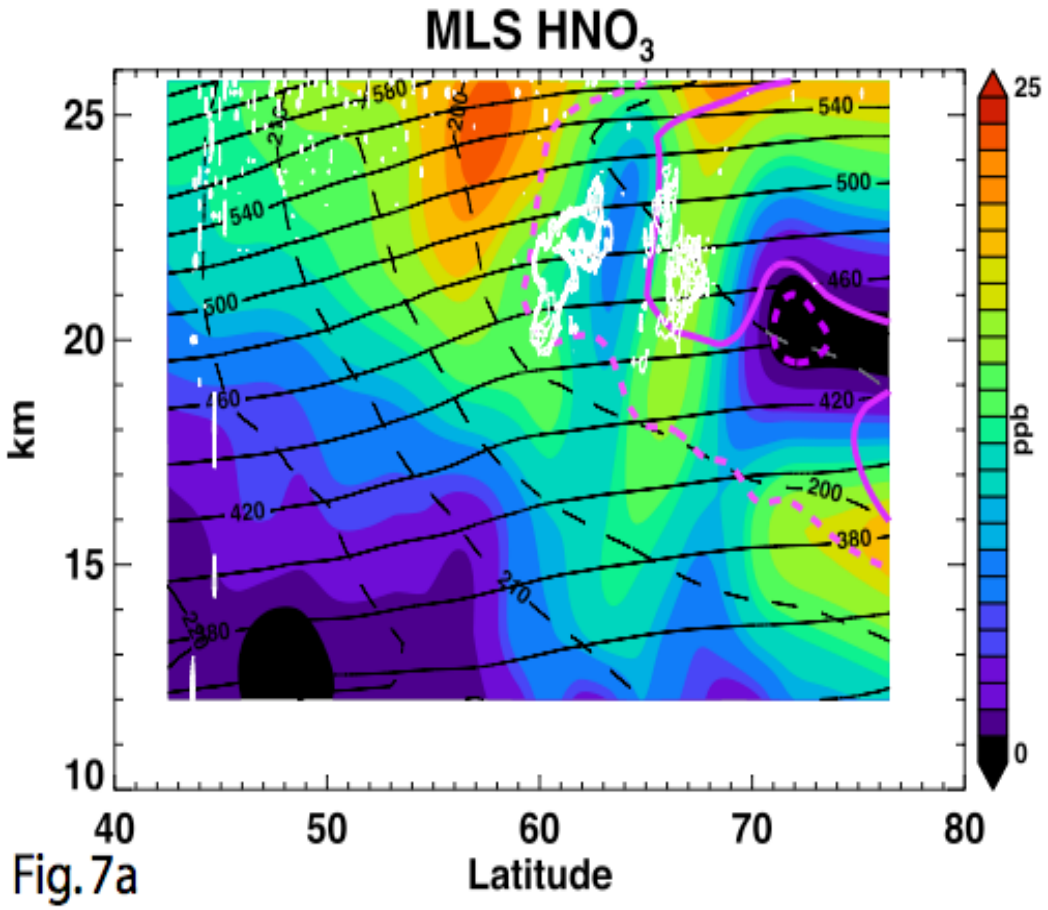
MLS HNO3
km
Latitude
ppb
25
20
15
10
40
50
60
70
80
0
540
500
460
420
380
200
240
560

Fig. 7a

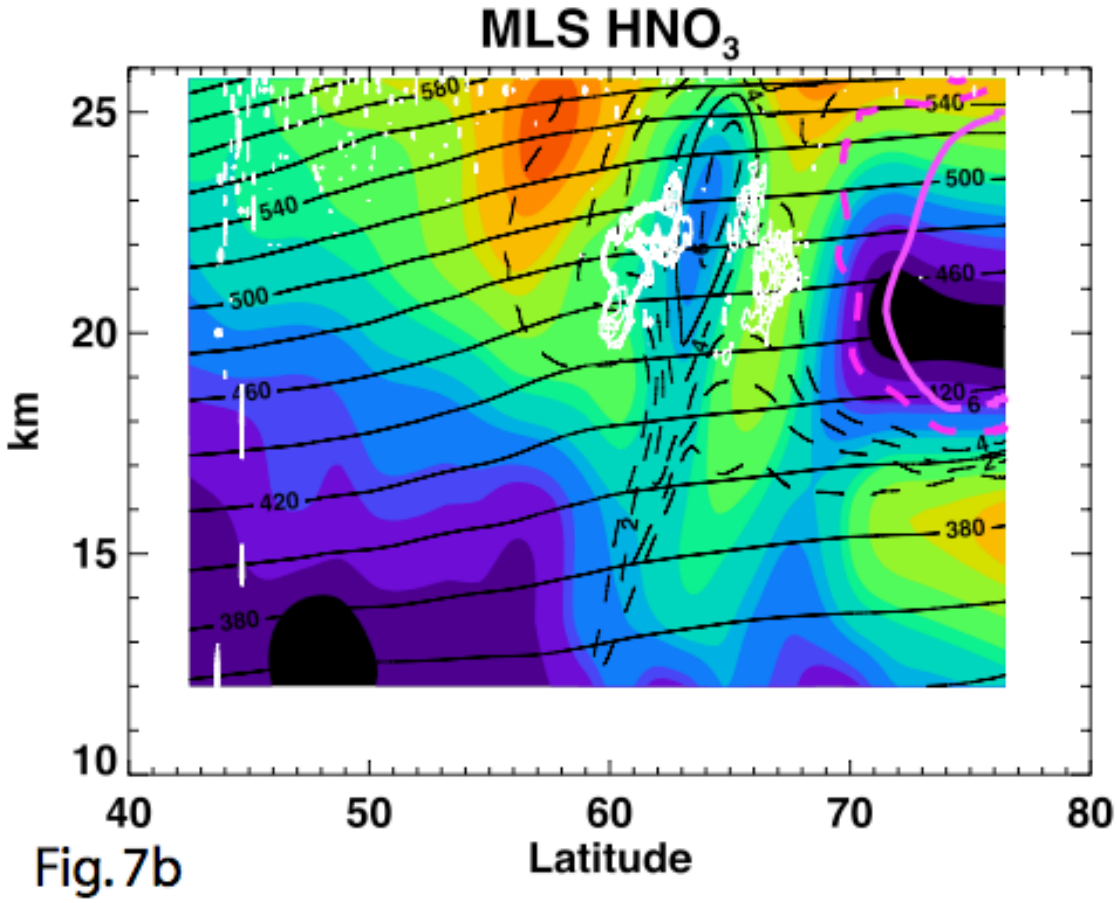
MLS HNO3
km
25
20
15
10
40
50
60
70
80
Latitude
560
540
500
460
420
380
540
500
460
20
6
4
2
380

Fig. 7b

MLS HNO_3 Jan 31, 2005

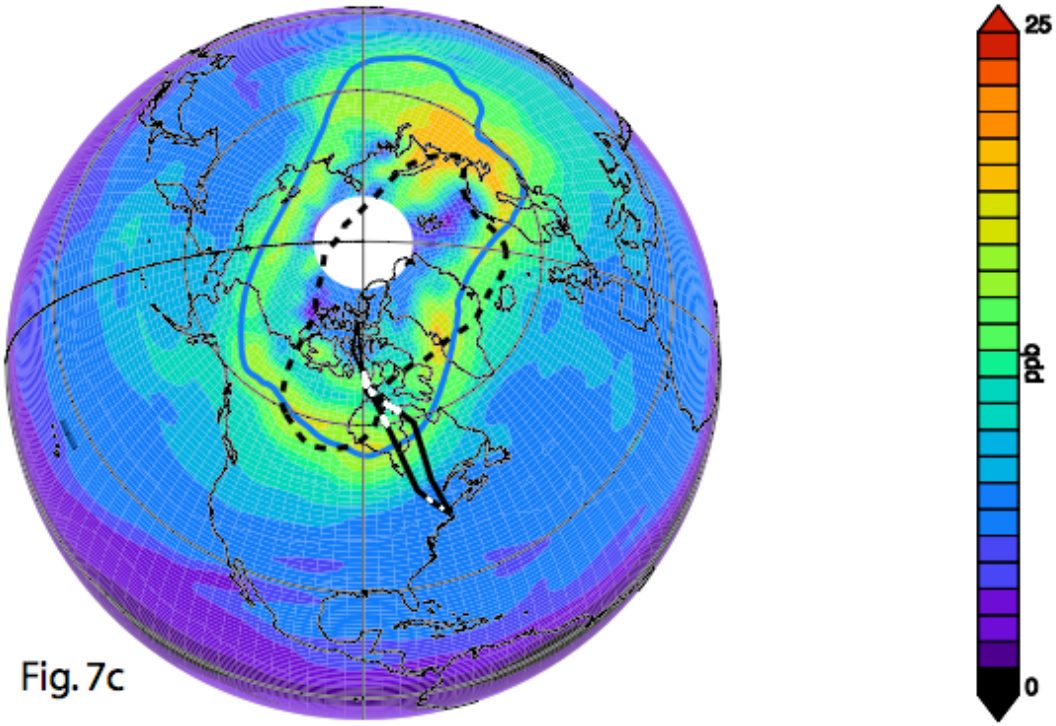

Fig. 7c

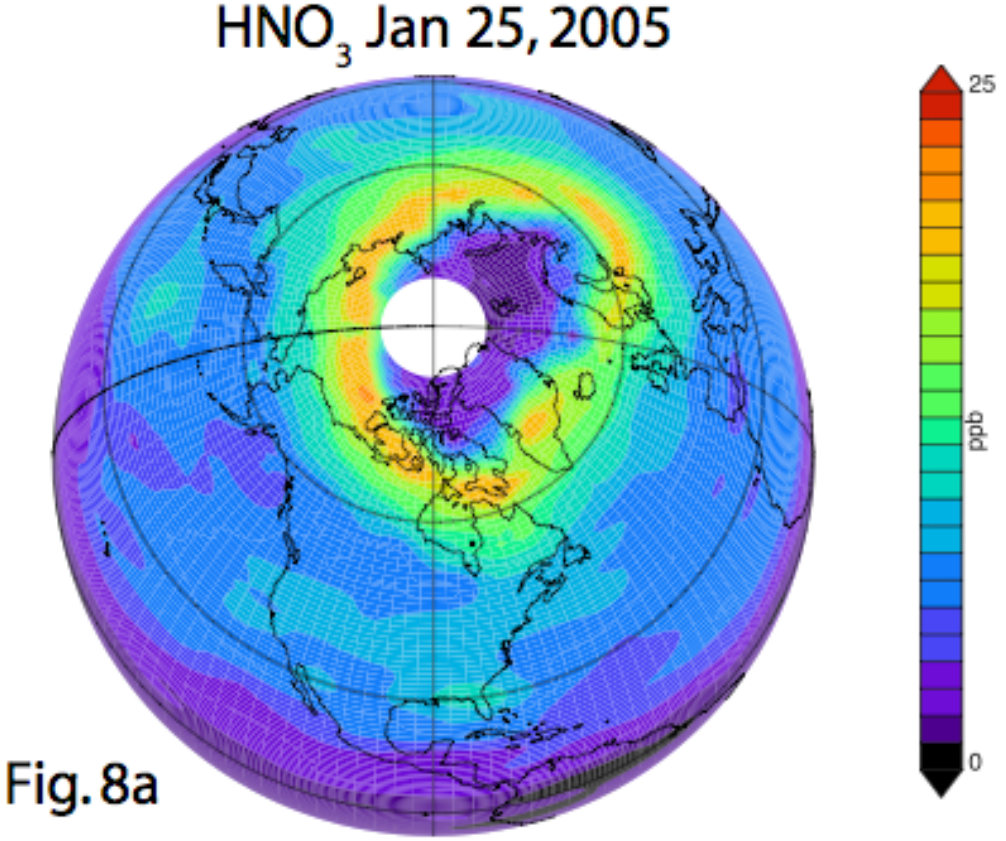

Fig. 8a

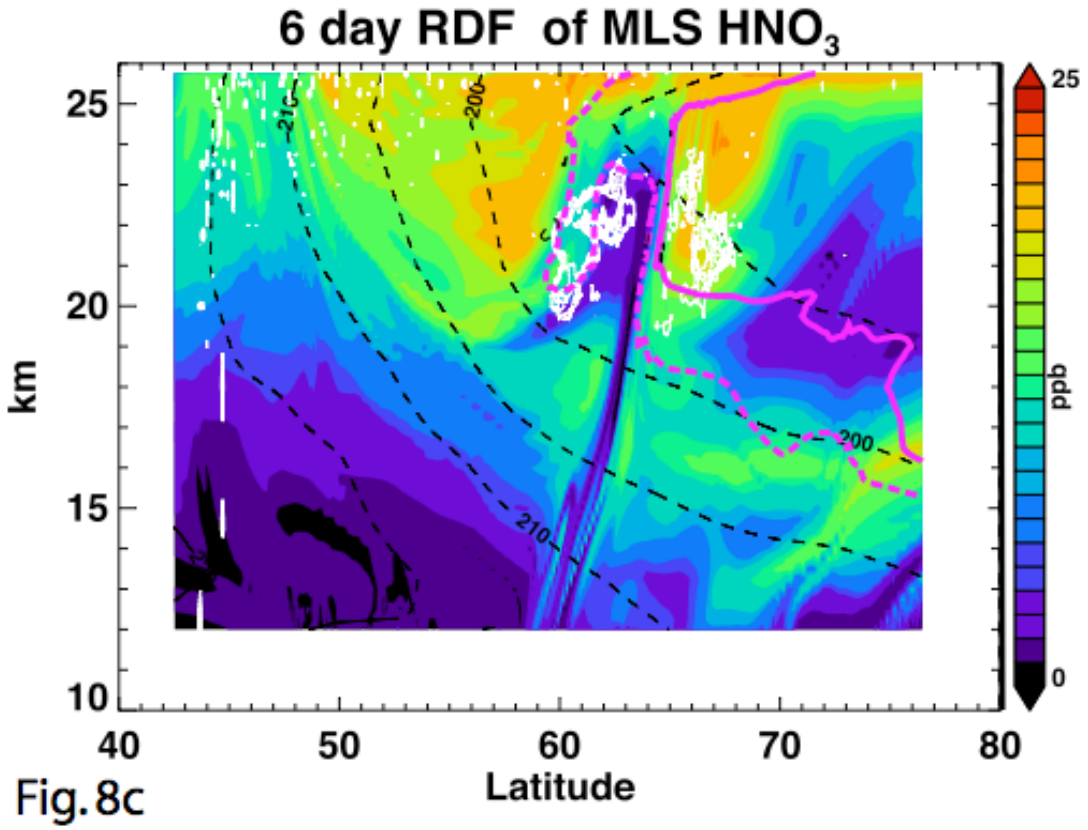
6 day RDF of MLS HNO3
km
25
20
15
10
40
50
60
70
80
Latitude
ppb
25
0
210
200
200

Fig. 8c

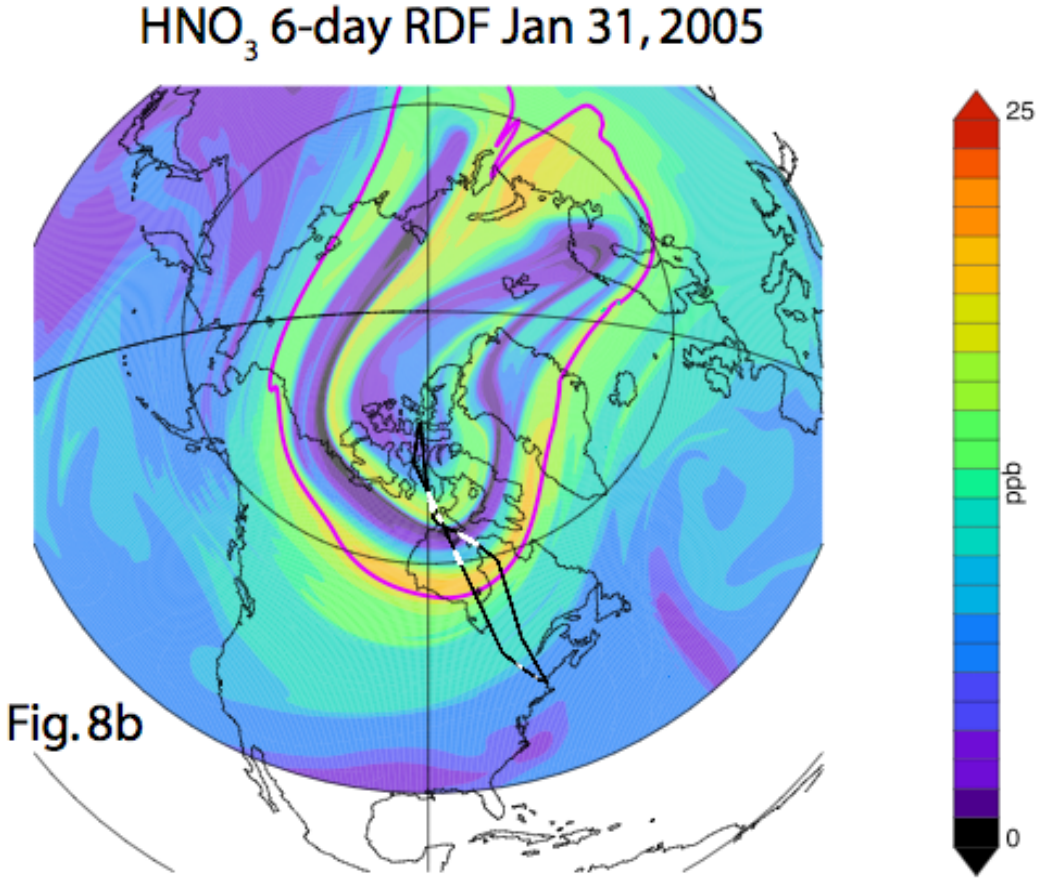

Fig. 8b

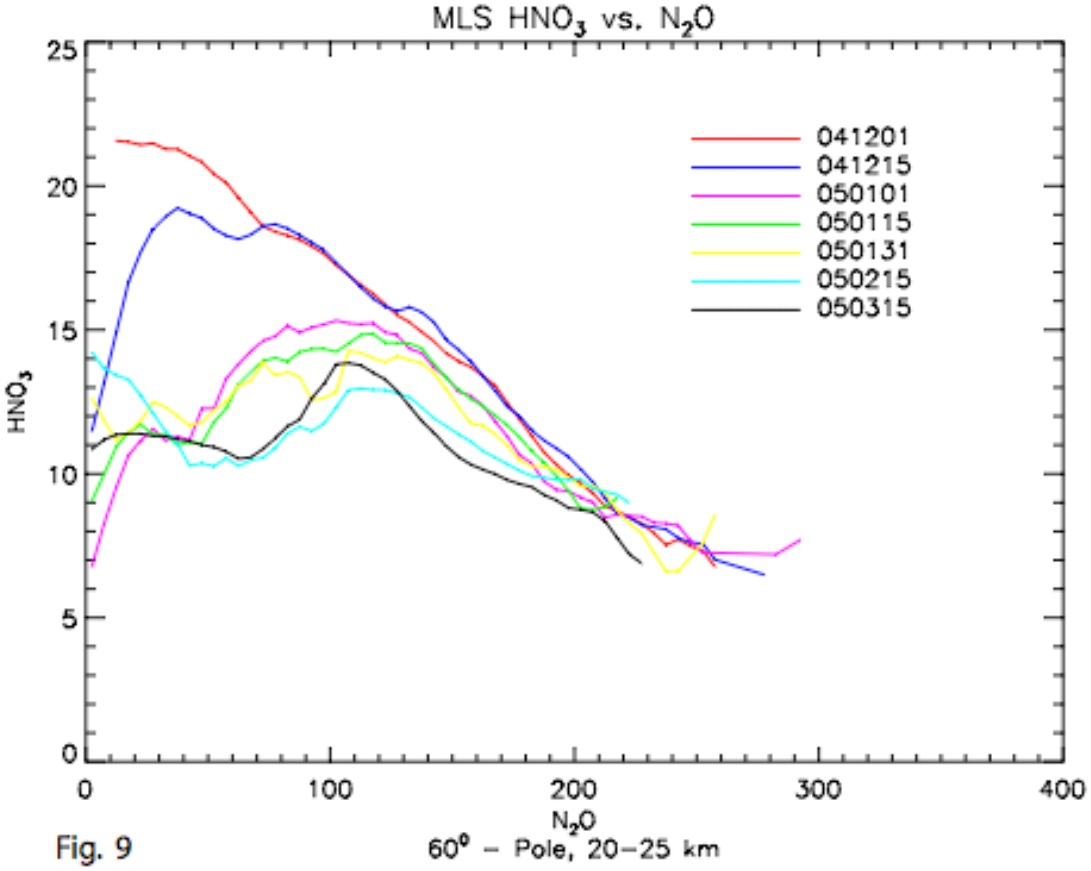

Fig. 9 60^0 – Pole, 20–25 km

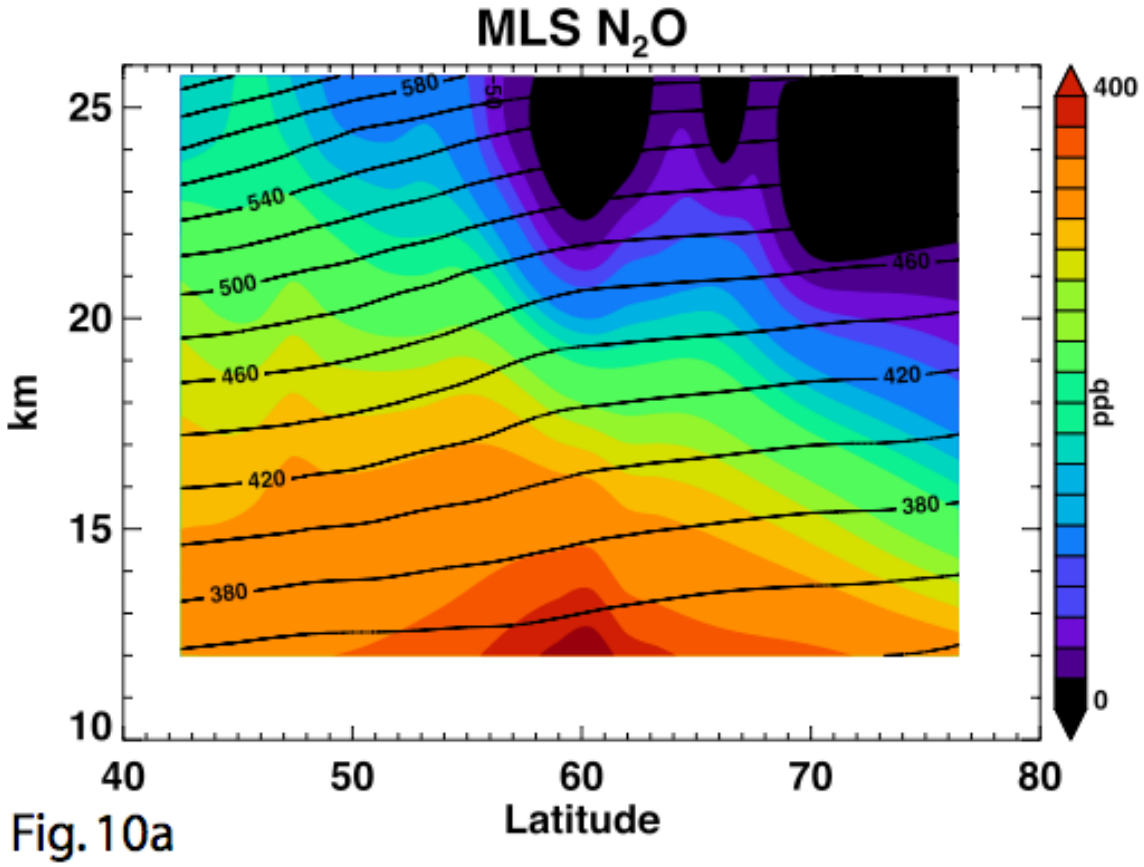
MLS N_2O
25
20
15
10
km
40
50
60
70
80
Latitude
580
540
500
460
420
380
460
420
380
400
ppb
0

Fig. 10a

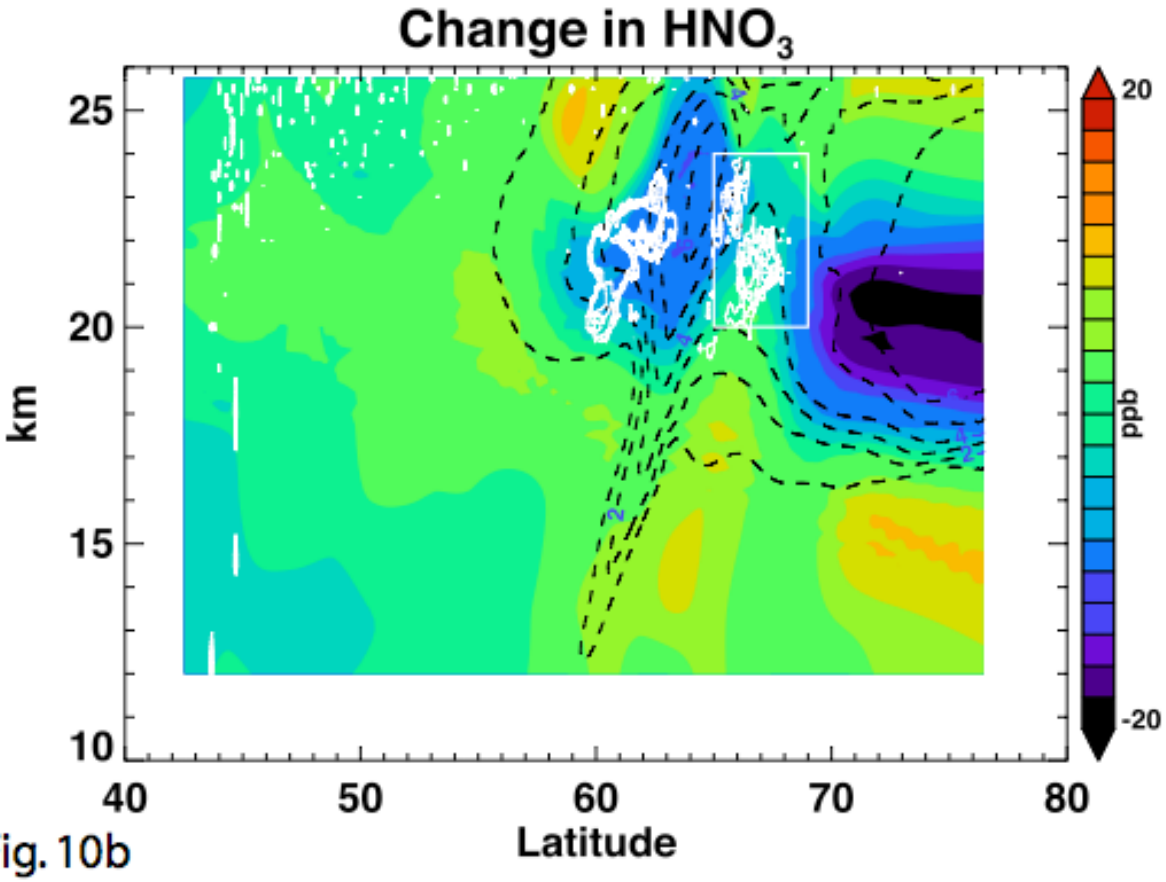

Fig. 10b

Change in HNO_3 Jan 31, 2005

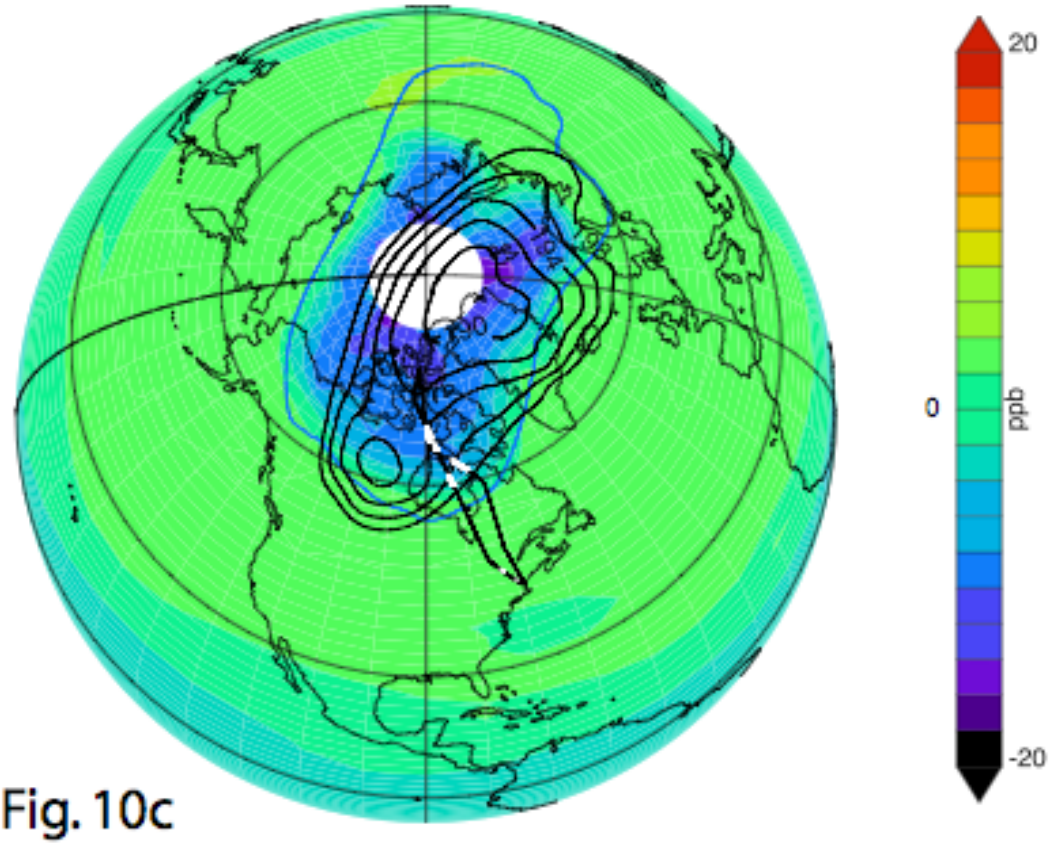

Fig. 10c

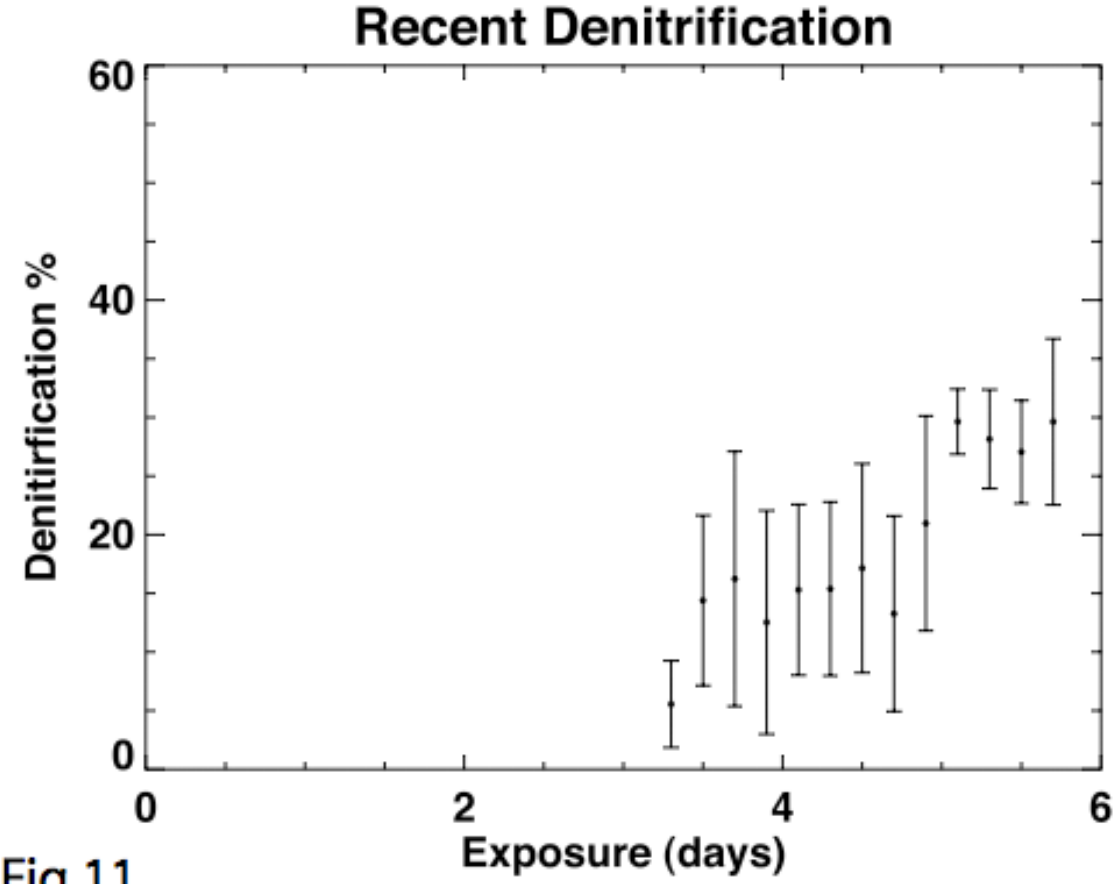
Recent Denitrification
Denitirfication %
60
40
20
0
0
2
4
6
Exposure (days)

Fig 11

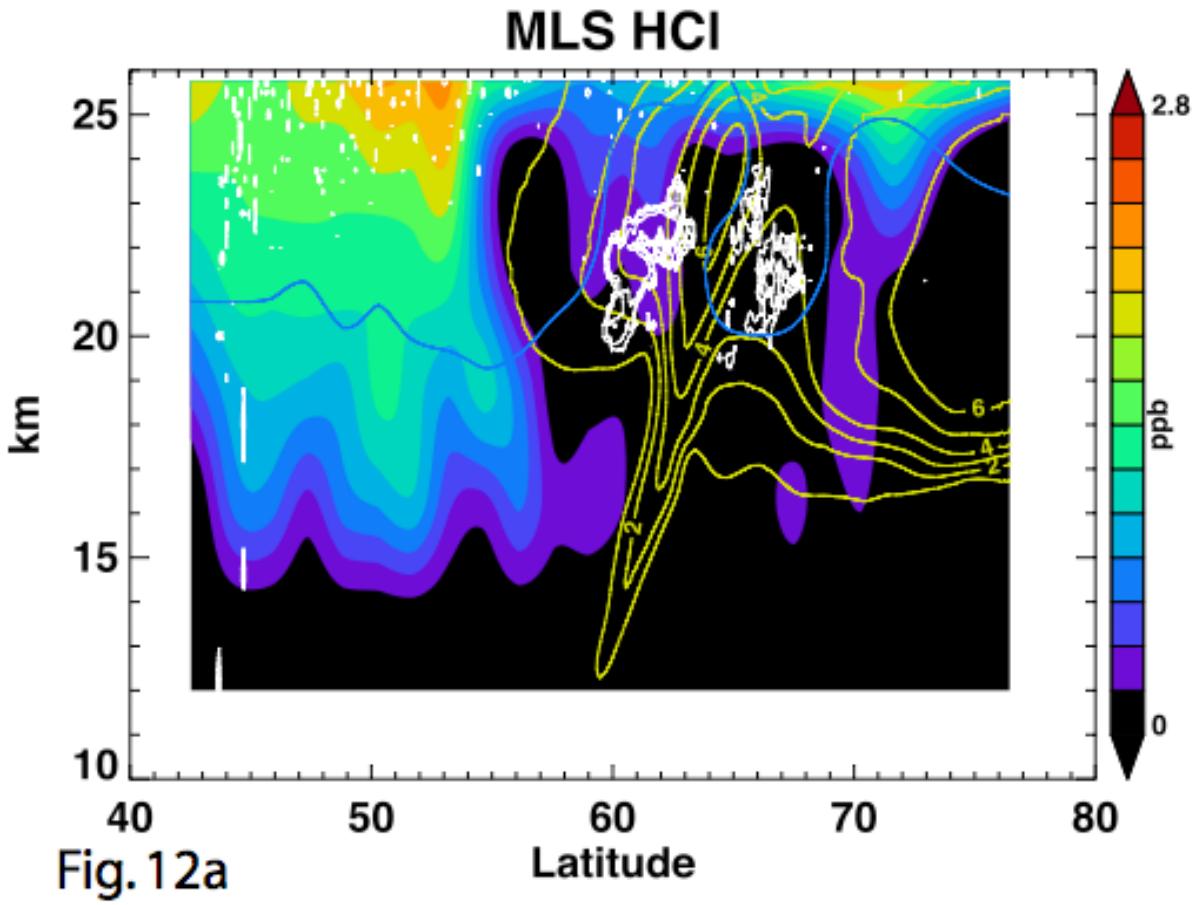

Fig. 12a

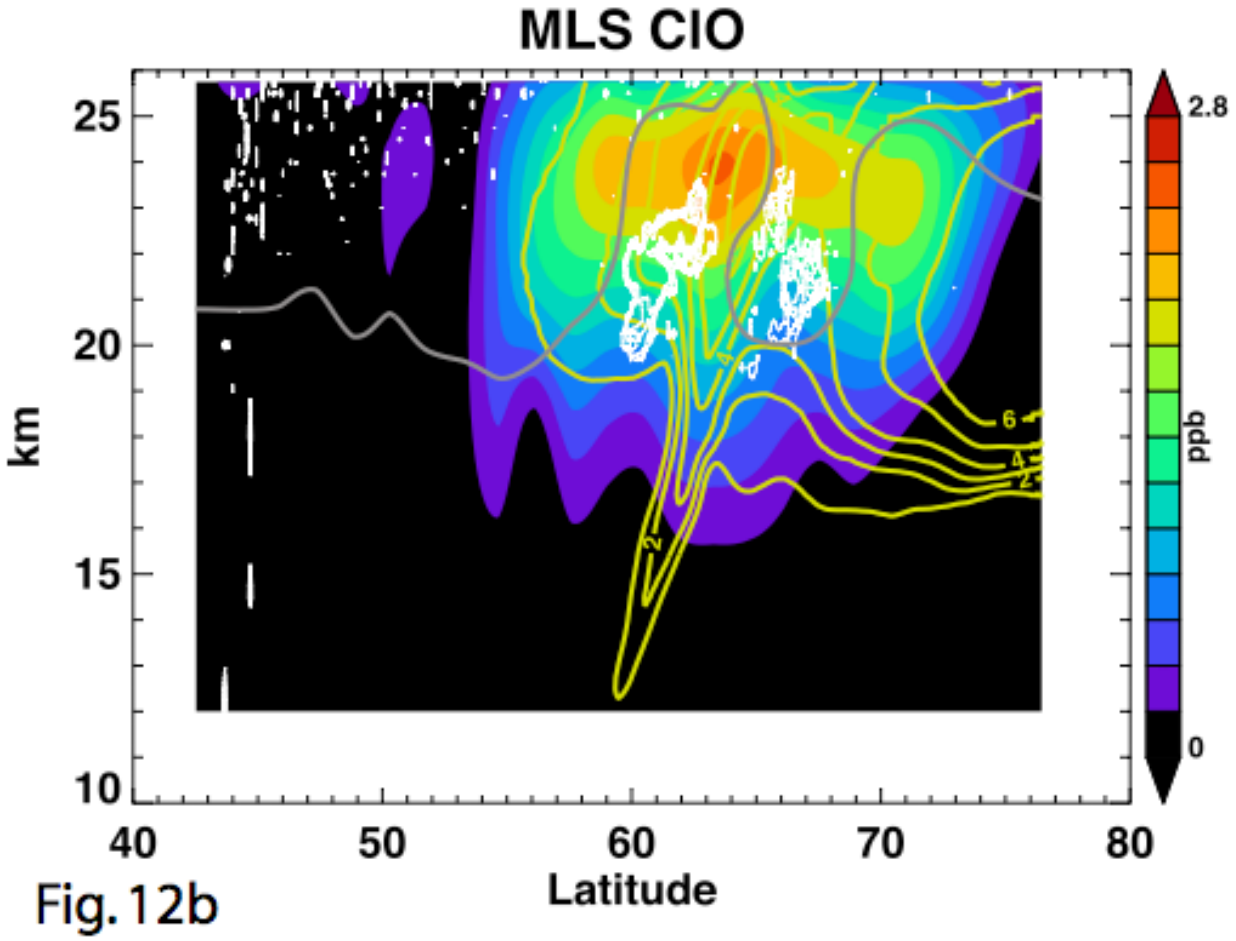

Fig. 12b

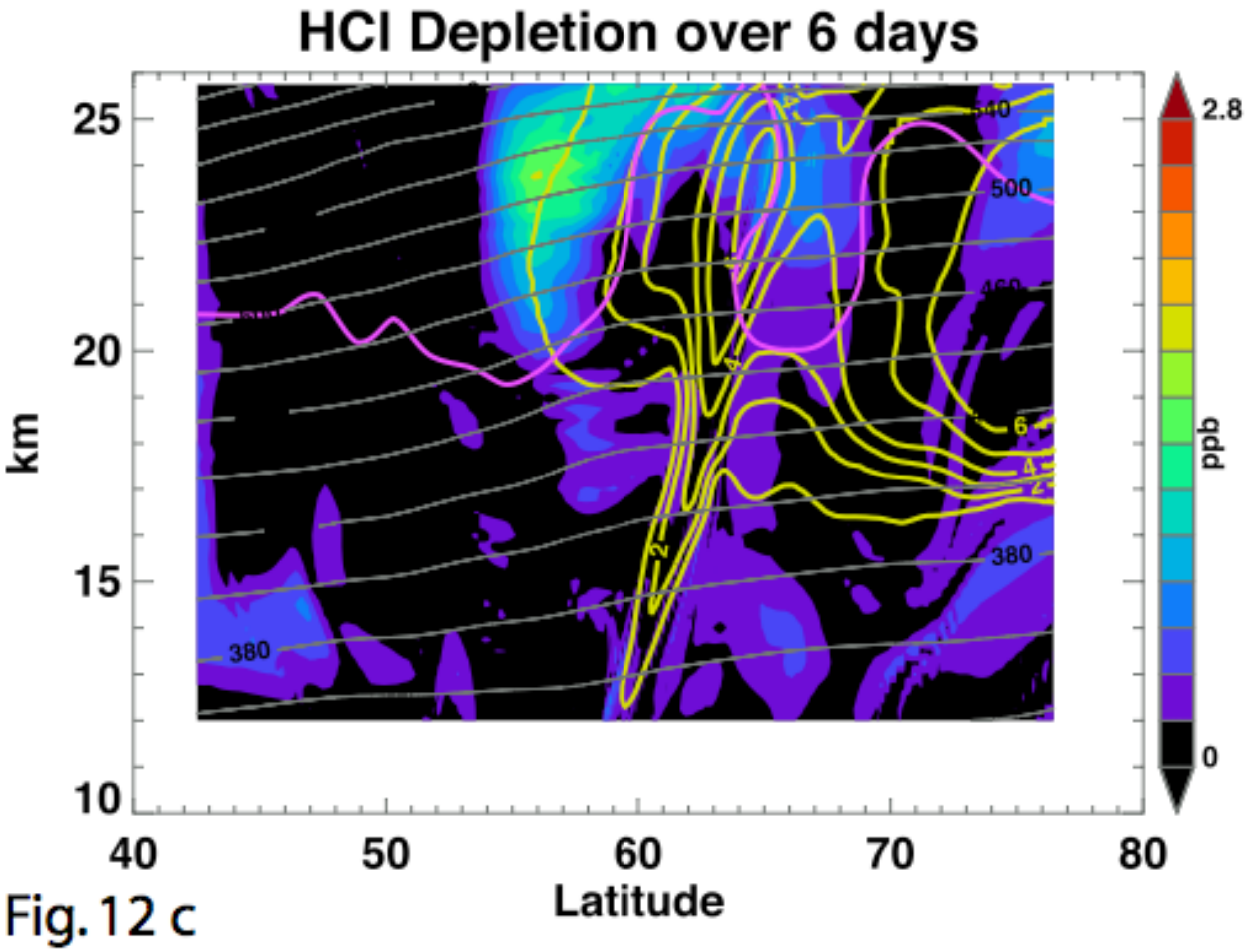
HCl Depletion over 6 days
25
20
15
10
km
40
50
60
70
80
Latitude
2.8
ppb
0
500
460
380
6
4
2
380

Fig. 12 c